On the Role of Physics in the Growth and Pattern Formation of Multi-Cellular Systems: What can we Learn from Individual-Cell Based Models?

Dirk Drasdo,[1,2,3,4] **Stefan Hoehme**[3] **and Michael Block**[5]

We demonstrate that many collective phenomena in multi-cellular systems can be explained by models in which cells, despite their complexity, are represented as simple particles which are parameterized mainly by their physical properties. We mainly focus on two examples that nevertheless span a wide range of biological sub-disciplines: Unstructured cell populations growing in cell culture and growing cell layers in early animal development. While cultured unstructured cell populations would a priori been classified as particularly suited for a biophysical approach since the degree to which they are committed to a genetic program is expected to be modest, early animal development would be expected to mark the other extreme—here the degree of determinism according to a genetic program would be expected to be very high. We consider a number of phenomena such as the growth kinetics and spatial structure formation of monolayers and multicellular spheroids, the effect of the presence of another cell type surrounding the growing cell population, the effect of mutations and the critical surface dynamics of monolayers. Different from unstructured cell populations, cells in early development and at tissue interfaces usually form highly organized structures. An example are tissue layers. Under certain circumstances such layers are observed to fold. We show that folding pattern again can largely be explained by physical mechanisms either by a buckling instability or active cell shape changes. The paper combines new and published

[1] Mathematics Institute and Center for Systems Biology, University of Warwick, Coventry CV4 7AL, UK.

[2] French National Institute for Research in Computer Science and Control (INRIA), Rocquencourt, B.P. 105, 78153 Le Chesnay Cedex, France; e-mail: dirk.drasdo@inria.fr.

[3] Interdisciplinary Centre for Bioinformatics, University of Leipzig, Härtelstr. 14–16, D-04107 Leipzig, Germany.

[4] Max-Planck-Institute for Mathematics in the Sciences, Inselstr. 22–26, D-0 4103 Leipzig, Germany.

[5] Institute for Theoretical Physics, Technical University of Berlin, D-10623 Berlin, Germany.

material and aims at an overview of a wide range of physical aspects in unstructured populations and growing tissue layers.

1. INTRODUCTION

After more than two decades of mainly focusing on genetic triggers and switches the role of mechanics and physical interactions in the control of growth and pattern formation in multi-cellular systems is attracting increasing interest (e.g. Refs. 1–5).

For example, both the saturation size and the shape of three dimensional multi-cellular aggregates growing in an embedding medium ("multi-cellular spheroids") depend on the mechanical properties of the embedding medium, namely, its rigidity.[6] In the experiments by Helmlinger *et al.*[6] the rigidity of the embedding medium was increased by increasing its amount of agarose. An increase of the agarose concentration leads to a smaller saturation size of the expanding multi-cellular spheroid.

Cells either on flat substrates,[7] or in epithelial cell layers of the lung[8,9] or the pancreas[10] may grow and divide faster if situated at positions of large local tissue curvature. Cells may also use mechanical stress to adjust their growth rate to the growth rate of other cells in a tissue sheet.[11] There are different ways in which a cell can control its physical properties and mechanically communicate with its environment depending on its state of differentiation, its type and on the properties of its environment.[1] For example, a cell can reorganize its cytoskeleton and thereby change its shape and mechanical rigidity. Or, a cell can control the number, placing and specificity of adhesion molecules which it uses to anchor in a substrate or to form contacts to its neighbor cells and thereby control the strength and specificity of its substrate and neighbor-cell contacts.[12]

Recently, more and more mathematical models are developed to explore potential explanations on the role of biomechanics in the control of morphogenesis and growth (e.g. Refs. 13–17). Mathematical models can contribute to distinguish between effects that can be explained purely by physical interactions and those effects that require (active) regulative changes of the cell behavior or the cell properties. However, the possible benefit of model simulations largely depend on in how far they can be experimentally validated.

A number of years ago the validation of predictions from mathematical models of multicellular systems was very difficult—if not impossible. This situation is rapidly improving now. The experimental abilities to collect information on the cell-biophysical, cell-biological and cell-kinetic properties have improved significantly in the last years. For example, the cell proliferation (cell division) activity can be determined by the markers Ki-67,[18] BrdU or Thymidin,[19] the apoptosis

(programmed cell death) by Tunnel assay,[18,20] the diffusion constant of cells by tracking labeled cells,[21] the elastic modulus of cells by optical stretchers,[22] atomic force microscopy (AFM),[23] or acoustic microscopy,[24] the strength of cell-cell and cell/substrate adhesion by AFM.[25,26] Recent cytometric (e.g. Ref. 27 and Refs. therein) and reconstruction methods of 3d tissues from 2d serial sections[28] provide the conditions to quantify experimentally obtained spatial-temporal labeling pattern in tissues and tissue morphotypes necessary for the comparison to the results of mathematical models. Moreover the technical abilities are crossing the borders between different disciplines. For example, methods that previously have only been used by cell-biologists such as cell-cycle labeling are now also used by other disciplines such as engineering science and combined with measurements on the mechanical stress within cell layers to identify the active and passive properties within multi-cellular systems.[7] This will facilitate to construct mathematical cell and tissue models that vice versa help to analyze further biological experiments given these models properly represent the relevant cell parameters. On the level of an individual cell these are for example cell-biological parameters such as the cycle time, the control of the cell cycle passage, apoptosis (programmed cell death) and cell-biophysical parameters such as cell material parameters, cell shape, and the strength and specificity of cell-cell and cell-substrate adhesion. The advantage of mathematical models is that they permit to test hypotheses free from uncontrolled or unknown experimental influences and to make predictions that help to select between competing hypotheses.

In this paper we illustrate by in-silico experiments that a number of experimental observations in different multi-cellular systems can largely be explained based on a description of cells mainly as physical objects capable of pursuing only a minimum of additional actions. The basic model-building strategy follows the same spirit as traffic simulations by agent based physical models:[29] starting with very simple models successively more complex regulation processes on the cellular and sub-cellular level are included. As long as the rules that underlie cell regulation and differentiation have not been understood, the predictive power of simulations of multi-cellular systems is limited. However, the point at which the experimental system behavior starts to deviate from the simulated behavior demarcates where cells might have changed their properties by regulation or differentiation; in so far simulations may help to find such points.

We partly review some recent work, and partly present complementary and new material. The basic model unit in most of our studies is an individual cell. In most biological examples we consider a model type in which each cell is parameterized by characteristic measurable cell-biological and cell-biophysical quantities. These models base upon a conceptual approach published some years ago.[30] We complement these by examples where each cell is considered as a point object on a lattice. Recent reviews on individual-based cell models, most of them defined on a lattice (cellular automata) can be found in Refs. 27, 31–35.

The multi-cellular systems we consider in this paper are 1. monolayers,[36–39] 2. multi-cellular spheroids[6,40–42] and 3. one-layered tissue structures in which the layer is not attached to a fixed surface; examples are multicellular structures in early development and epithelial interfaces.

By growing monolayers we here mean cell populations growing on a flat substrate. Depending on the cell type and the substrate used they may form a sparse distribution of cells, a one-cell-thick layer attached to the substrate, a quasi-monolayer in which some cells do not have contact to the substrate anymore or even multi-layered structures. Besides the growth kinetics and the morphotype (the spatial distribution) also the critical surface dynamics of monolayers have been explored.[36]

If those cell types that can grow independent of substrate contact are exposed to liquid medium they form multi-cellular spheroidal aggregates.

Examples for the formation of highly organized one-layered structures are blastula formation and gastrulation in species that form a one-cell-thick blastula such as *sea urchin* and *synapta digita*,[43,44] and epithelial tissues that form a one-cell-thick interface such as intestinal crypts,[45–47] the lung[8] or the basal layer of the mucosa.[48]

The paper is organized as follows. We firstly present selected examples on growing unstructured cell populations. This part is subdivided in growing mono-layers and multi-cellular spheroids. For growing monolayers we subsume findings on their growth kinetics (i.e., how the population size and their spatial spread evolves in time), the morphotype of the expanding cell populations and the critical surface dynamics of expanding cell populations. In the same section we outline how the morphotype of a cell clone changes if it grows in a co-culture of (non-dividing) cells which we believe can easily be tested by experiments. As a step towards how invasive pattern may form, we study how mutations that affect the model parameters such as the length of the cell cycle time, the probability of programmed cell death (apoptosis) or the sensitivity towards contact inhibition of growth may affect the multicellular phenotype. Mutations have been shown to cause genetic heterogeneity of cells in tumors and of micrometastases.[49] The subsection is followed by a model of growing cell populations in liquid suspension i.e., of cell populations not attached to any substrate. The multi-cellular aggregates formed under this condition are called "multi-cellular spheroids." The second main section focuses on a simulated scenario in early development and presents results on the modeling of buckling and folding events in one-layered tissues. Finally we close the paper by a summary and a discussion.

2. MONOLAYERS AND MULTICELLULAR SPHEROIDS

Within the last decades biological in-vitro (as opposed to in-vivo, i.e., in the living organism) models of in-situ tumors and micrometastasis have been developed and extensively studied in order to characterize their growth dynamics under

various conditions.[40,41] Commonly used techniques are monolayer cultures where cells grow on a Petri dish coated with proteins and liquid media containing specified quantities of small molecules such as salts, glucose, amino acids, and vitamins, and furthermore growth factors and transferrin, which carries iron into cells.[50−53] In-vitro cell cultures are important experimental tools in understanding and analyzing the mechanisms involved in the growth of cell populations. Treatment strategies for a number of diseases may be tested in-vitro with respect to their efficiency and their toxicity before being applied to in-vivo systems. This in particular involves testing drug, radiation, and chemotherapy strategies against cancer.[42] Their advantage over in-vivo systems is that they can easily be manipulated.

Many types of normal animal cells need anchorage to grow and proliferate. When normal fibroblasts or epithelial cells, for example, are cultured in suspension they round off and usually do not divide.[54] In order to permit division they need to be anchored in the substrate by focal contacts. Focal contacts are links of the actin cytoskeleton by cell-surface matrix receptors (integrins) to extracellular matrix (ECM) molecules, such as laminin or fibronectin. The binding of ECM molecules to integrins leads to the local activation of intracellular signaling pathways that can promote the survival, growth and division of cells. As a consequence normal cells usually stop division at confluence, i.e., if the cells form a closed monolayer on the floor of the culture dish. In the next sub-section we will firstly introduce a model to explain the observed growth pattern on flat substrates. Tumor cells are often able to grow and divide anchorage-independent. I.e., they can be grown in suspension, not being attached to a substrate, where they form growing spherical aggregates (tumor spheroids). Whether cell lines basically grow as monolayers or also expand perpendicular to the substrate depends on whether certain mechanisms that control growth and apoptosis work properly. Different cell lines originating from the same tissue may grow very differently. E.g., while HCT116 cells, a Human colon carcinoma cell line, grow mainly as a monolayer, WiDr cells, a Human colon adenocarcinoma cell line, quickly expand into the direction perpendicular to the plane of the substrate. After the study of perfect (one-cell-thick) monolayers we explore the effect of simulated knockouts of growth mechanisms and show that the phenotype in this case can dramatically change. This is followed by co-culture simulations of cell clones growing in an environment of non-dividing cells, the critical surface dynamics generated by cells at the monolayer border and the possible effects of mutations that affect the kinetic cell parameters on the monolayer kinetics and phenotype. The second sub-section IIB will focus on tumor spheroids.

2.1. Monolayers

2.1.1. Perfect One-Cell-Thick Monolayers on a Flat Substrate

Bru et al.[36,55] have grown two-dimensional tumor monolayers from C6 rat astrocyte glioma cells. They observed a linear growth of the tumor diameter L

(A)   (B)
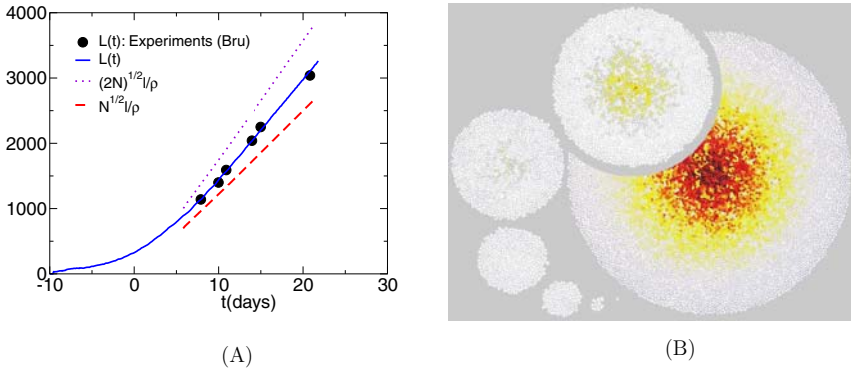
Fig. 1. A: Growth kinetics of C6 rat astrocyte-cells in monolayer cultures. Experimental observation of the diameter L (black dots) and the simulated curve (straight line). Note that there is an initial exponential growth of $L(t)$. The dotted and dashed line are calculated from the simulated cell population size $N(t)$. The dashed line denotes $\sqrt{N}l/\varrho$ where $\varrho = 0.91$ is the optimum packing density of discs in two-dimensional space and l is the cell diameter. The dashed line would be expected to collapse with the $L(t)$ if no cell would be in the proliferation cycle and if all cells were packed at maximal density. The dotted line denotes $\sqrt{2N}l/\varrho$ which would be expected if all cells were immediately before division hence having twice the volume of a non-proliferating cell. By a least-mean square fit one finds that the average cell size of the cell population is $\approx 1.15\,l$ i.e., between the minimum cell size l and its maximum $\sqrt{2}l$. (For the simulations we used the basic model described in the text.) B: Typical monolayer growth scenario. Shown are snapshots at $N = 10, 100, 250, 1000, 2500$ and 12500 cells, respectively. The lighter the cells the shorter is their cell cycle time. Above a certain monolayer size the main cell proliferation activity is close to the border while the cell proliferation activity in the interior is very small. The parameters in this simulation were $l = 10\,\mu$m (Bru, priv. communic.), $\tau = 18$ h (Bru, priv. communic.), $E = 400$ Pa,[56,57] $D = 4 \times 10^{-13}$ cm^2/s, $\delta = 0.2\ell$, $\epsilon = \epsilon_s$, (obtained from $\varrho_m \approx 5 \times 10^{14}$/m^2,[25,58] $W_s = 25k_BT$), $F_T \approx 6 \times 10^{-16}$ J[59,60] (see text for details).

with time t (Fig. 1A) even if the monolayer was covered with additional nutrient medium. Thus even though all cells were in contact to the nutrient medium the growth was not exponential but linear. Moreover, although in monolayer cultures no shortage of glucose (or oxygen) occurs, a characteristic proliferation pattern forms above a certain population size with the highest proliferation activity close to the tumor boundary.[55] This suggests that the division of non-boundary cells may be repressed by a form of contact inhibition. This finding has stimulated us to study whether the growth kinetics and spatial growth pattern can be explained by a mechanical form of contact inhibition.

The quantitative information available on growing cell populations is still insufficient to set up a model that reproduces every minute detail of in-vitro tumors. Rather we follow the view of Ref. 61 and illustrate how a (mechanistic) model that is based on characteristic features of individual cells is capable of giving at least a partial explanation of the growth dynamics of in-vitro tumors. Our model approximates each cell by an elastic, sticky particle of limited compressibility

and deformability capable of active migration, growth and division; each model parameter can in principle be experimentally determined.

The major model features and assumptions are summarized below (additional technical details can be found in Appendix A, alternative model variants are discussed below).

The basic model:

(A1) Since isolated cells in cultures or suspensions often have a spherical shape we assume each model cell to be spherical directly after cell division. Cells that do not continue to grow and divide ("to proliferate") are assumed to maintain the spherical shape. Proliferating cells grow and deform into a dumb-bell during mitosis until they divide into two spherical daughter cells of equal size (Fig. 2(A)). The initial orientation of the dumb-bell axis is random within the plane of the substrate (see also assumption A4 for further explanation).

(A2) Cells in contact can form adhesive bonds. With decreasing distance between cell centers (e.g., upon compression) the contact area between them increases and with it, the number of adhesive bonds, resulting in an increasing attractive interaction. On the other hand, if cells in isolation are spherical, an increasing contact area is accompanied by an increasing deformation which results in a repulsive interaction. Furthermore cells under physiological conditions have only a moderate compressibility. We model the combination of attractive and repulsive interactions by the interaction energy (Fig. 2(C)):

$$V_{ij} = \begin{cases} \epsilon \left(\frac{2\tilde{d}_{ij}(t)}{\delta} + \sqrt{\frac{\epsilon_s}{\epsilon}} \right)^2 - \epsilon_s & \text{if } -\delta \le \tilde{d}_{ij}(t) \le 0 \\ \infty & \text{if } \tilde{d}_{ij} < -\delta \\ 0 & \text{otherwise.} \end{cases} \tag{1}$$

$\tilde{d}_{ij} = d_{ij} - (R_i + R_j)$ where d_{ij} denotes the distance between the nearest spheres of the neighboring dumb-bells i, j (here, $R_i = R_j = R$). $\epsilon_s \approx \varrho_m A_{ij} W_s$ is the cell-cell adhesion energy. W_s is the energy of a single membrane receptor bond of adjacent cells, A_{ij} the contact area between cells i, j and ϱ_m denotes the density of cell-cell adhesion receptors in the cell membrane. The term $\epsilon(\ldots)$ in the first line of Eq. (1) represents the elastic contributions. $\epsilon \approx El\delta^2/8$ includes the cell elastic modulus E of the cell, and $\delta/2$ is the range over which a cell may be stretched or compressed. The cell diameter of a cell immediately after division is $l \approx 2R$ (while we define that the cell has an incompressible core with radius $R - \delta/2$, see Fig. 2).

(A3) In the absence of chemotactic signals, isolated cells in suspension or culture medium have been observed to perform a random walk.[21,60]
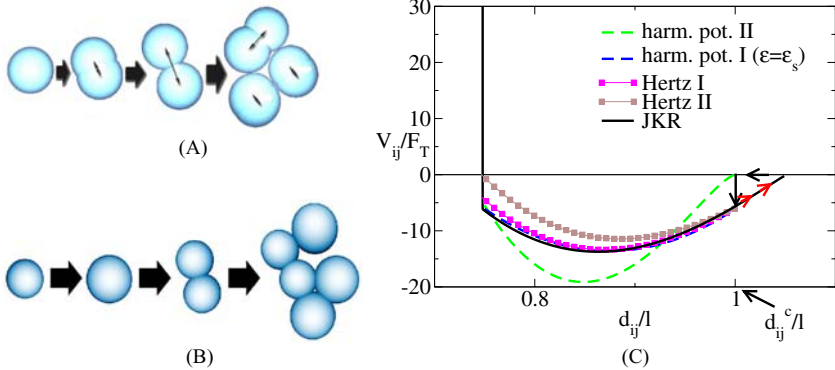
Fig. 2. A and B: Illustration of the two used cell division algorithms, C: Interaction potential energy between the nearest spheres of the neighboring dumb-bells i, j (here, $R_i = R_j = R$). A: During cell division, a cell deforms from a perfect sphere into a dumb-bell in small steps $\delta_a \ll l$. The pictures show the incompressible core of the cells i.e. the cells in their maximal compressed state. Each incompressible dumb-bell cores has the radius $R - \delta/2$ and the size (diameter) $l - \delta$. An uncompressed and undeformed cell directly after division is spherical with diameter $l = 2R$. Our algorithm mimics a linear increase of cell mass during the passage of a cell through the cell cycle in agreement with the experimental observations.[62] B: Different from the division algorithm in (A) the radius is first increased from $R \rightarrow 2^{1/3} R$ to mimic the doubling of the cell volume followed by a cell deformation into dumb-bells at constant volume. C: Interaction potential energy between the nearest spheres of the neighboring dumb-bells i, j (here, $R_i = R_j = R$). The shape of V_{ij} reflects the limited compressibility and deformability of the cells and contains direct cell-cell adhesion. Three different models are shown, a harmonic-like interaction energy, a Hertz-like approach[63] and the Johnson-Kendall-Roberts (JKR)-model (e.g. Refs. 64–66) of adhesive, deformable, isotropic and homogeneous elastic spheres. Within a realistic range for the effective energy F_T that models the migration activity of the cells and of the Young modulus within a range of 300–600 Pa, however, the approaches result in very similar shapes for the interaction energy for $d_{ij}/l \leq 1$. (For embryonic cells Beysens et al.[59] found $F_T \approx 2-8 \times 10^{-15}$ J, experiments by Schienbein et al.[60] with granulocytes suggest that $F_T = \sim 10^{-17}$ J.) For $d_{ij} > l$ the JKR-model shows a hysteresis behavior if cells detach (red arrows in the upper figure where detachment occurs $d_{ij}^c = l$). For illustration purposes the Hertz I/Hertz II-potentials and the harmonic potential I (where $\epsilon_s = \epsilon \approx -7.5\,F_T$) were lowered by -6 (note that the dynamics is determined by the energy differences only). The other parameters were the same for the Hertz II and the JKR interaction energy curves. For the Hertz I-curve the surface tension was assumed to be 20% above those for the Hertz I and JKR curves (we used an surface receptor density of 10^{15} m^{-2}[25,58] and a binding strength of $W_s = 15-25\,k_B T$ for each receptor).

We model this by a stochastic component in the movement of each cell which we characterize by the cell diffusion constant D.

(A4) While in mechanical contact to other cells, proliferating cells exert a pressure on their neighbors. The neighboring cells try to escape this pressure by moving against the friction caused by the other neighbor cells and extracellular material (e.g. matrix). The stronger the friction, the slower the cells move. We simulate a friction-dominated stochastic

dynamics driven by physical interactions by the standard Metropolis algorithm[67] with a proper definition of timescales (e.g. Refs. 30, 68, 69). Note that the movement may be active or passive or both. The observations in Ref. 7, however, suggest that on a flat substrate cells migrate rather than being pushed by dividing cells. The algorithm uses the interaction energy (A2, Eq. (1), see-also Fig. 2C), that can directly be related to forces. In our two-dimensional monolayer simulations we perform on average one translation trial of size ξ and one orientation trial of angle $\delta\alpha$ per cell within each time period Δt and accept it with probability $P_a = 1$ if $\Delta V^{\text{tot}} = V_{t+\Delta t}^{\text{tot}} - V_t^{\text{tot}} < 0$ and with probability $P_a = \exp(-\Delta V^{\text{tot}}/F_T)$ otherwise. Here, $V^{\text{tot}} = \sum_{i<j}^N V_{ij}$ summarizes the attractive and repulsive cell-cell interactions, V_{ij} denotes the interaction between cells i and j (Fig. 2B). Every $n_g \gg 1$ translation and orientation trials, one growth trial of size δa uniformly distributed in $[0, \delta a_{\text{max}})$ is performed. F_T is a reference energy[59] analogous to the thermal energy $k_B T$ in fluids or gases (T: temperature, k_B: Boltzmann const.). α is the rotation angle of the dumb-bell axis in the substrate plane. (For our three-dimensional simulations in Figs. 3, 5, and 9 we considered rotations around three space-fixed axes by an angles $\delta\alpha_i$ with $i = 1, 2, 3$ according to the algorithm of Barker and Watts (see Ref. 70).) ξ and $\delta\alpha$ are random variables distributed uniformly in the intervals $\xi \in [0, \xi_{\text{max}})$ and $\delta\alpha \in (-\delta\alpha_{\text{max}}, \delta\alpha_{\text{max}})$ respectively. Each translation step trial is performed into a random direction. $\xi_{\text{max}} \ll l$, $\delta\alpha_{\text{max}} \ll \pi$. In order to use the Monte Carlo method for kinetic simulations we have defined time scales for each of the processes growth, division, migration and rotation. Consider migration as an example. Firstly we build a list containing all cells at a certain point of time to insure that no cell is omitted for a migration trial. We successively choose all cells from the list (in random order) and perform one migration trial per cell. We perform this procedure consisting of 1. setting up the list and 2. performing precisely one migration trial per cell n_g-times in time intervals of Δt before performing a growth or division trial for each cell in the same way (building a list, performing one trial per cell). The size and frequency of the migration and growth (and division) trials is chosen in such a way, that the diffusion constant and the cycle time of isolated cells are correctly reproduced so that a simulation mimics a realistic time development of the multicellular configuration (further technical details on how the step size variables ξ_{max} and δa_{max} as well as n_g are related to measurable quantities such as the cycle time τ and the diffusion constant D can be found in Appendix A). The use of the Monte Carlo method is motivated by the observation that after each growth step all cells move to relax the configuration at least into a local

equilibrium;[30] the procedure used here corresponds to the numerical integration of a master equation for the time development of the multi-cellular configuration (compare Ref. 71).

(A5) We assume an average intrinsic cell cycle time to be influenced at the level of individual cells by nutrients, regulatory factors and mechanical stress. We denote τ as the average intrinsic cell cycle time of an isolated cell not affected by physical interactions with neighboring cells. We assume that a cell within a multicellular aggregate can grow only if it is not deformed or compressed greatly. In our model a growth trial is accepted only if the cell-cell distance (or more precisely, the distance between the centers of neighboring dumb-bells) doesn't fall below the minimal distance $d_{ij}^{\min} = 2R - \delta$. Consequently the observed cell cycle time of deformed cells is typically larger than the intrinsic cycle time.

(A6) We start our simulation with a single cell.

It is not necessary to model glucose or oxygen explicitly, since in the cultured monolayer experiments by Bru *et al*.[36] nutrients are equally accessible to all cells.

In order to relate the numbers on the computer to "real" biological situations we introduce a length, a time and an energy scale and refer all model parameters to groupings of these reference scales.

We will firstly present simulation results obtained by simulations with this model. This is followed by a discussion of a modification of some of the model assumptions, namely of a modification of the cell division algorithm (A1), of the cell-cell interaction energy (A2) and of the cell movement algorithm (A4).

Figure 1B shows a typical time series of the monolayer morphology and a snapshots of the layer-like proliferation pattern for population sizes of $N = 1$ to $N = 12500$ cells. The highest proliferation activity is close to the monolayer boundary while in the interior almost no proliferation can be found in agreement with the experimental observations. As shown in Fig. 1A the time development of the monolayer diameter is also in good agreement with the experimental observations for C6 rat astrocytes.

As long as a monolayer is sufficiently small the number of cells that have to rearrange if a cell in the monolayer interior grows or divides is small. Accordingly a growing cell in the monolayer interior is in general able to exert a sufficiently strong force on its neighbors to push these aside or stimulate them to actively migrate away. Since glucose and oxygen are not limiting, cells divide everywhere in the monolayer hence the cell population size grows exponentially fast. The cell cycle time τ can be experimentally determined from the slope of the growth curve in the initial exponential growth regime of the cell population size (Fig. 9C illustrates this for multicellular spheroids). Our model predicts that above a certain monolayer size cells sufficiently far in the monolayer interior become jammed between so many surrounding cells that they are neither capable of pushing their

neighbors aside nor is active migration of surrounding cells fast enough to generate sufficient space for interior cells to divide. This results in a large stress inside the monolayer which relaxes toward its boundary only within a small surface layer where cells are able to divide. In this regime, $dL/dt = v \approx 2\Delta L/\tau$, where ΔL is the width of the proliferation zone (white in Fig. 1B) and τ is the cycle time. Our explanation is supported by the observation of Bru *et al.* (priv. comm.) that almost each cell was in close contact to its neighbors. Alternatively, one may think of contact inhibition initiated by the interaction of cell surface receptor molecules. In this case, if cell-cell attraction is present, only the outermost cells of the monolayer would be able to divide in which case the growth velocity would be $2l/\tau \approx 1\,\mu$m/h (l: cell diameter), i.e. smaller than the value of $5.8\,\mu$m/h found by Bru *et al.*[36] Note that this case corresponds to the assumption of the Eden model[72] in which cells occupy sites of a lattice, at most one cell per lattice site, and cell division can only occur onto adjacent free lattice sites.

Another possible alternative would be that the boundary cells detach from the monolayer and freely migrate away from the monolayer center. Such a behavior can be observed for invading tumor cells.[73] In this case the boundary of the monolayer would not be sharp but disperse. Such a behavior is qualitatively modeled by the Fischer-KPP-equation in which the local density of cells is assumed to change by logistic growth and diffusion (e.g. Refs. 74, 75). However, the observed shape of the cell aggregates by Bru suggests that at least for HT-29 cells[55] and for C6 rat astrocyte cells (Bru, priv. communication) it is not the migration of detached cells that is responsible for the observed linear growth regime.

From the above reasoning the expansion velocity can be changed by mechanisms that either modify the thickness of the proliferation layer ΔL or modify the cell cycle time (τ). The thickness of the proliferation layer can be increased in the model by decreasing the Young modulus or the sensitivity for contact inhibition by increasing δ (since both lead to an increase of the force necessary to cause an exceeding of the deformation or compression threshold necessary to stop cell growth), or increasing the migration activity (for example, by the parameter n_g; since this facilitates cells to escape a critical deformation or compression by migration).

Model variants:

We have considered a number of model variants to test the robustness of the findings. (AV1) Instead of modeling the cell deformation and the cell growth (i.e. the process which increases the cell volume) at the same time by a deformation of a cell into a dumb-bell with concomitant volume increase as shown in Fig. 2A, we have tested a cell division algorithm in which the cell remains spherical until it has doubled its volume (i.e. until it has adopted a diameter of $2^{1/3}l$) followed by a deformation into a dumb-bell at constant cell volume Fig. (2B). This division algorithm originally introduced in Ref. 30 distinguishes between interphase and
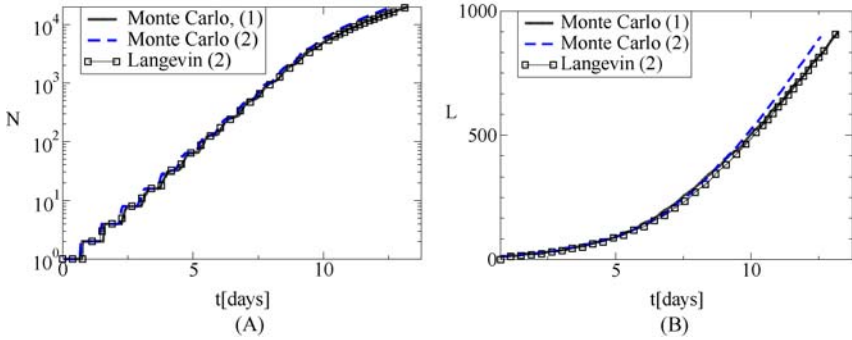
Fig. 3. Comparison between Langevin and Monte Carlo simulation for a selected parameter set. (1) denotes the cell division algorithm of Fig. 2A, (2) the cell division algorithm in Fig. 2B. A: Population size $N(t)$. B: Diameter growth $L(t)$. The model parameters were (in both simulations, a JKR-model was used): $l = 10\,\mu$m, $\tau = 18$ h, $D = 10^{-11}$ cm^2/s, $E = 450$ Pa, $\nu = 0.4$, $\varrho_m = 10^{-15}$ /m^2, $W_s = 25\,k_B T$, $F_T = 10^{-16}$ J, and for Langevin: $\gamma = 0.1$ Ns/m, $\gamma_\parallel^{(iy)} = \gamma_\perp^{(iy)} \approx 0.03$ Ns/m for $y = j, s$ (details see text).

mitose phase. The interphase subsumes the first three sub-phases, G_1, S, G_2 of the cell cycle.[76] During the mitosis phase the mitotic spindle forms and the cell subsequently divides. This process lasts about 2 h and is much shorter than the interphase (the total cell cycle length is usually about 24 h).[76] We found that this modification has (almost) no influence on the growth pattern (Fig. 3).

(AV2) Instead of using a simple harmonic-type interaction energy one may use other models. If we approximate cells by adhesive, deformable, isotropic and homogeneous elastic spheres, then suitable models are the classical Hertz-model[63] extended by a term that takes into account cell-cell adhesion[77,78] or the Johnson-Kendall-Roberts (JKR)-model (e.g. Refs. 64–66) which takes into account the hysteresis effect that occurs due to cell elongation if cells are pulled apart (compare Fig. 2(C) for both models).

In Fig. 2(C) we represent the interaction energy of these two alternative models that are calculated using the following relations:

(AV2.1): The extended Hertz-type interaction energy is

$$V_{ij} = (R_i + R_j - d_{ij})^{5/2} \frac{1}{5\tilde{E}_{ij}} \sqrt{\frac{R_i R_j}{R_i + R_j}} + \epsilon_s. \qquad (2)$$

The first term on the rhs. models the repulsive, the second term the adhesive interaction.

$$\tilde{E}_{ij}^{-1} = \frac{3}{4}\left(\frac{1 - \sigma_i^2}{E_i} + \frac{1 - \sigma_j^2}{E_j}\right). \qquad (3)$$

Here, E_i, E_j are the elastic moduli of the cells i, j, σ_i, σ_j the Poisson ratios of the spheres. This takes into account that a homogeneous, isotropic elastic body

is completely characterized by two independent material constants, for example the Young modulus and the Poisson ratio.

(AV2.2): The force $F_{ij} \equiv |\underline{F}_{ij}(d_{ij})|$ in the JKR-model has to be calculated numerically from the implicit equation:

$$\delta = \frac{a^2}{\tilde{R}} - [16\pi\hat{\gamma}a/(3\tilde{E}_{ij})]^{1/2}, \tag{4}$$

where

$$a^3 = \frac{2\tilde{R}}{\tilde{E}_{ij}}[F_{ij} + 3\pi\hat{\gamma}\tilde{R} + [6\pi\hat{\gamma}\tilde{R}F_{ij} + (3\pi\hat{\gamma}\tilde{R})^2)]^{1/2}]. \tag{5}$$

$\tilde{R}^{1-} = \frac{1}{R_i} + \frac{1}{R_j}$ and $d_{ij} = R_i + R_j - \delta$ (i.e., $\delta = \delta_i + \delta_j$ is the sum of the deformation along the axis between the centers of the closest spheres of the dumbbells of cell i and cell j), for $\tilde{E}_{ij}^{-1}$ see Eq. (3). $\tilde{\gamma} \approx \varrho_m W_s$, where $\varrho_m \approx 10^{15}$ m$^{-2(25,79)}$ is the density of surface adhesion molecules in the contact zone and $W_s = 15 - 25 k_B T$ is the binding energy of a single bond. Eq. (5) has to be solved implicitly to give $a(F_{ij})$. The value of a is plugged into Eq. (4) to give $\delta(a)$ and, by $d_{ij} = R_i + R_j - \delta$, $d_{ij}(a)$. Plotting F_{ij} vs. d_{ij} yields $F_{ij}(d_{ij})$, which cannot be given explicitly but can be easily fitted by a polynomial (we used a polynomial of degree three). From this, the JKR-energy V_{ij} can be investigated by integration using the $\underline{F}_{ij} = -(\partial V_{ij}/\partial d_{ij})(d(d_{ij})/dx_i, d(d_{ij})/dy_i, d(d_{ij})/dz_i)$. The corresponding interaction energy is shown in Fig. 2C.

As Fig. 2C illustrates, the shape of the different interaction potential energies is very similar for the harmonic-like, the Hertzian-like, and the JKR-interaction energy if two cells adhere. The most important difference of the JKR-model to the Hertz-model is the hysteresis effect that results from the strong attraction: when two spheres approach each other they spontaneously form a contact area of finite size at a distance $d_{ij} = 2R$ while at $\lim_{\epsilon\to0} 2R + \epsilon$ they had no contact. If they are pulled apart, however, they still have contact at distance $\lim_{\epsilon\to0} 2R + \epsilon \leq d_{ij} \leq d_{ij}^c$ (Fig. 2C). This leads to a marked difference in situations in which cell detachment becomes important as we show in the next subsection where we consider a piling up of monolayers.

Eventually, to insure quantitative predictions beyond qualitative tendencies, it is necessary to measure all cell-biophysical and cell-biological parameters in the same biological system to determine the cell-cell (and cell-substrate) interaction energy.

(AV4:) The Metropolis algorithm may be viewed as a numerical integration of a master equation for the probability density distribution to find the multi-cellular configuration in a state characterized by the cell variables such as their positions, orientations, sizes etc.[71] A more intuitive way to model the cell movement may be by equations of motion for each individual cell. We have studied Langevin-type

equations of motion for each cell i given by

$$\left(\gamma + \underline{\underline{\Gamma}}^f_{is}\right)\frac{d\underline{x}^i}{dt} + \sum_{j\, nn\, i} \underline{\underline{\Gamma}}^f_{ij}\left(\frac{d\underline{x}^i}{dt} - \frac{d\underline{x}^j}{dt}\right) = \sum_{j=1}^{N} \underline{F}^{ij} + \underline{\eta}^i(t). \qquad (6)$$

Here, $\underline{x}^i$ is the position of the center of cell i, γ denotes an effective friction coefficient that determines the speed of an isolated cell subject to an external force. We have used the division algorithm in Fig. 2B for which we found that each proliferating cell spends most of its time in the spherical growth phase (and not in the dumb-bell-deformation phase). For this reason we neglected rotations of dumb-bells by a torque. For spherical cells, $\underline{\underline{\Gamma}}^f_{iy} = \gamma_\parallel^{(iy)}\underline{n}_{iy}\underline{n}_{iy} + \gamma_\perp^{(iy)}(\underline{\underline{E}} - \underline{n}_{iy}\underline{n}_{iy})$. Here $y = j$ denotes cell-cell, and $y = s$ cell-substrate interactions. $\underline{n}_{iy} = \frac{\underline{x}_y - \underline{x}_i}{|\underline{x}_y - \underline{x}_i|}$. $\underline{n}_{iy}\underline{n}_{iy}$ here denotes the dyadic product i.e. is a 3×3-matrix. $\gamma_\parallel^{(iy)}$ and $\gamma_\perp^{(iy)}$ are the parallel and perpendicular friction constants, respectively (for example, $(\underline{\underline{E}} - \underline{n}_{is}\underline{n}_{is})\,\underline{v}$ is the projection of $\underline{v}$ onto a plane perpendicular to $\underline{n}_{is}$, so if $\underline{v} \perp \underline{n}_{is}$, then the friction is solely given by $\gamma_\perp^{(cy)}$). To calculate $\underline{x}_y - \underline{x}_i$ if $y = s$ denotes a flat substrate, approximate the flat substrate by a sphere and consider the limit where the radius of the sphere diverges.

In (radially) expanding monolayers the velocity of neighboring cells is very similar due to the circular monolayer shape so that the friction between cells may be neglected and hence the sum on the lhs. of Eq. (6) be dropped. The autocorrelation function of the noise then is $\langle \eta^i_m(t)\eta^j_n(t') \rangle = A\delta_{ij}\delta_{mn}\delta(t - t')$. If the cell-cell friction is neglected in the autocorrelation function of the noise and if $\gamma_\perp^{(is)} = \gamma_\parallel^{(is)}$, then $A = 2(\gamma + \gamma_\perp^{(is)})F_T$. If the cell-cell friction term is not neglected and if $\gamma_\perp^{(iy)} = \gamma_\parallel^{(iy)}$ for both, cell-cell ($y = j$) and cell-substrate-friction ($y = s$), then $A \approx 2(\gamma + \gamma_\perp^{(is)} + \sum_j \gamma_\perp^{(ij)})F_T$.[77,80] Note that $\gamma_\parallel$ and $\gamma_\perp$ include the information about the contact area. By the Stokes friction one can relate the friction constants with the radius of the contact area and the viscosity of the medium.

Figure 3 shows a comparison between the Metropolis-method and the numerical integration of the Langevin equations (note that the simulations shown in Fig. 3 are with the cell-cell friction term). The curves show a reasonable agreement. For very small step sizes ξ_{max} (at large n_g between subsequent growth trials) so that $|\Delta V_{ij}| \ll F_T$, the curves should collapse.

We also studied the size of clones of successively born cells which be believe reflects the competition of cells for free space. Our model predicts that nearby cells in the monolayer can form sub-clones of largely different sizes as a consequence of a competition of growing and dividing cells for free space (Fig. 4). Those cells which are under slightly smaller compression can on the average more easily grow and divide than those cells which are under larger compression. At the monolayer border, usually the cells at the tip of the border are under smaller compression
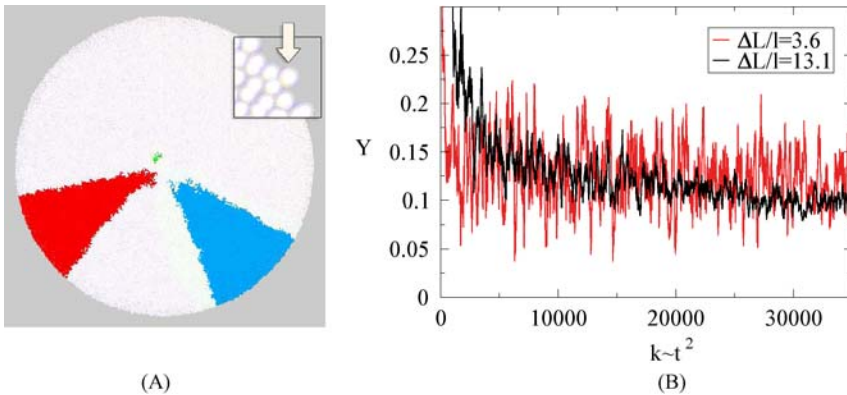
Fig. 4. Subclone sizes. (A) The three clones (red, blue, green) emerged from cells that were born immediately one after the other. The average clone size is expected to behave as $\langle N_k \rangle = q(N - k)/N_p$ where k enumerates all cells in chronological order from $k = 1, 2, \ldots, N_p$ is the number of proliferating cells and q is a fit parameter. $N_p = k$ in the exponential ($k \propto \exp(t/\tau)$) and $N_p = k^{d_s/d} \Delta L/l$, in the surface growth ($k \propto t^d$) regime, where d_s is the global surface dimension, and d the dimension into which the tumor is expanding (for monolayers, $d_s = 1$, $d = 2$). By definition, $N_{k=1} = N$. For the red, blue and green clone approximately the same clone sizes would be expected while the observed clone sizes show significant differences. The arrow within the magnification shows a cell at a locally convex position of the surface that has a larger probability to form a large clone. (B) shows the gliding average $Y \equiv \overline{N}_{k,\Delta k} N_p/(N - k) \approx q$ (where we have approximated $\langle N_k \rangle$ by $\overline{N}_{k,\Delta k}$ with $\Delta k = 200$ and chosen $N_p = \kappa^{1/2}$) which fits well the mean-field form although the true sub-clone size shows large fluctuations in the surface growth regime if the proliferative activity is concentrated at the monolayer boundary. Here, ΔL has been defined by $v = dL/dt \equiv 2\Delta L/\tau$ where v is the expansion velocity of the monolayer and τ the intrinsic cycle time (set to $\tau \approx 19$ h). v can be obtained from $L(t)$ The cell diameter was assumed to $l = 10 \, \mu$m. The diffusion constant of isolated cells for the curves in Fig. 4(B), were $D = 1.4 \times 10^{-13}$ cm^2/s (blue curve) and $D = 2 \times 10^{-12}$ cm^2/s (black curve), respectively. (For comparison: for the monolayer growth curve in Fig. 1A, $D \approx 4 \times 10^{-13}$ cm^2/s. The other parameters are as in Fig. 1.)

(compare the arrow in the magnification of Fig. 4A) which is why their average cycle time length is usually smaller than the cycle time length of cells at concave positions of the border so that their clones usually out-compete clones which are formed by cells at convex border positions. One way to test this observation of clonal competition found in our computer simulation is to label individual cells by markers such as BrdU.[19] BrdU is passed on the daughter cells in case a cell divides.

2.1.2. Piling up of Cells on a Flat Substrate

Many of the epithelial cell populations which are subject to cell-substrate contact dependent proliferation and anoikis grow in a cell culture to confluent

cell monolayers[81–83] and simultaneously establish a cell polarity. Epithelial cells form inner and outer surfaces of the body.[84] Anoikis is a special type of selective programmed cell death that normally occurs if cells loose contact to the substrate.[85] Confluent cell monolayers form a one-cell-thick layer which covers the total area of the culture dish. The introduction of different oncogenes into cultured epithelial cell lines affects their signal transduction pathways.[86–88] In cell lines which normally form cell monolayers this can result in a break down of the epithelial cell polarity due to changes of the cellular adhesion properties[87] and/or prevents anoikis interrupting apoptotic signaling pathways.[88] Thereby it may enable anchorage independent growth, which is characteristic for many tumor cell lines.[89,90] The accumulation of such cells at confluence can lead to the formation of multilayers[87] or to the formation of spheroidal aggregates.[88] To explain these phenotypic differences between non-transformed and transformed cells biologists are focusing on the molecular mechanisms to understand how molecular signals from other cells or the substrate are transduced from the cell surface into the cell and affect the genetic control of cell proliferation and death.[86–88] As shown for endothelial cells, another critical determinant that switches cells from life to death and between proliferation and quiescence may be cell shape.[91] Epithelial cells are also able to sense changes within the local micro-environment by sensing the degree of their own extension or compression, and thereby couple shape changes to cell migration and proliferation.[92] Hence, some of the effects of cell contact formation and release during epithelial organization can be directly attributed to the physical interaction between individual cells and their neighbors, and between individual cells and their substrate.[77]

Cells in the interior of the monolayer experience a force from surrounding proliferating cells. Since monolayers are not completely flat but show small spatial fluctuations as a consequence of the stochastic growth and re-arrangement processes the force that an interior cell experiences from its surrounding cells is not completely parallel to the substrate. If the outward pointing force component of the total force that is exerted on a cell perpendicular to the plane of the monolayer overcomes the cell-substrate adhesion strength then cells may be pushed out of the layer (Fig. 5). This occurs in particular for cell lines which are either insensitive to contact inhibition or for which contact inhibition is completely switched off. Usually cells that loose substrate contact do not proliferate anymore (anchorage-dependent proliferation) and after a period of several hours undergo apoptosis (anchorage-dependent apoptosis: anoikis). In Fig. 5 we study successive knock-outs of (I), contact inhibition, (II). anchorage-dependent proliferation in addition to I and (III) anoikis in addition to II. As long as anoikis is still present a quasi-monolayer is maintained and again a surface growth regime with $L \propto t$ forms. Only if anoikis fails to work a significant piling up perpendicular to the plane of the substrate occurs (Fig. 5).
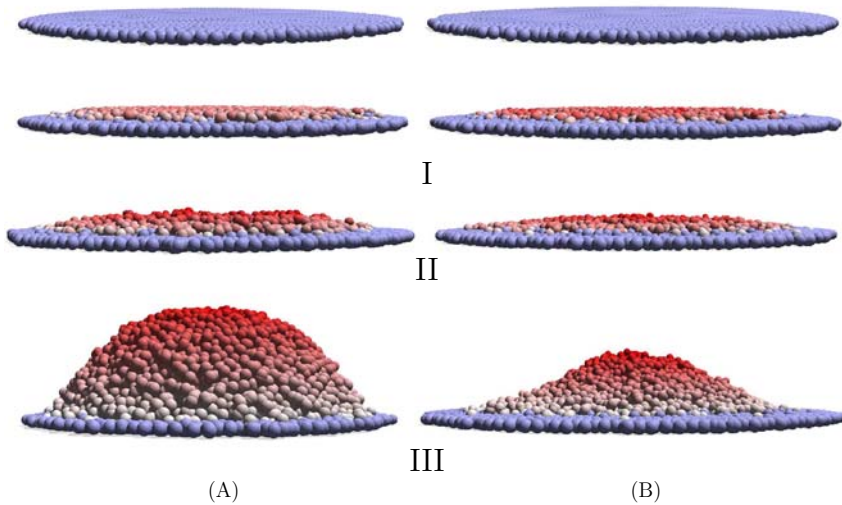
Fig. 5. Destabilization scenario of a monolayer adhered to a flat substrate in simulations by the basic model using the Hertz-type interaction AV2.1 (A) and the JKR-interaction energy AV2.2 (B). The color is a relative measure of how far the cells are above the substrate (blue: direct substrate contact, red: far above the substrate). The numbers (I), (II), (III) denote knocked-out control mechanisms, namely (I) contact inhibition: a cell in which this mechanism is knocked out is assumed to not stop to proliferate even if a critical compression or deformation threshold is overcome, (II) in addition to (I), anchorage-dependent proliferation: if this mechanism is absent cells do not stop to proliferate if they have lost substrate contact, and (III) in addition to (II), anchorage-dependent apoptosis (anoikis): if this mechanism is knocked out cells do not undergo apoptosis after they lost substrate contact while cells under normal control die a few hours after loss of substrate contact. (The same scenario have been found in a slightly different model in which the cell migration and the change of cell volume both have been modeled by a Langevin equation and a Hertzian-interaction energy have been used; for details, see Ref. 77.) The parameters in the Hertz and the JKR-model are the same. As the consequence of the hysteresis in the JKR-interaction energy, much less cells detach from the substrate for the JRK-interaction than for the Hertz-type, interaction. For growth in perfect one-cell-thick monolayers (uppermost case) the differences are negligible. The parameters are: $l = 10\,\mu\mathrm{m}$, $\tau = 18\,\mathrm{h}$, $E = 450\,\mathrm{Pa}$, $\mu = 0.4$, $D = 1.27 \times 10^{11}\,\mathrm{cm}^2/\mathrm{s}$, $\varrho_m = 10^{15}/\mathrm{m}^2$, $W_s = 25 k_B T$, $F_T = 10^{-16}\,\mathrm{J}$.

For the simulated knock-outs we used both, an extended Hertz-model (Eq. (2)) and the JKR-model (Eqs. (4) and (5)). The qualitative scenario is the same independently of whether the Hertz-or JRK-model is used. The hysteresis that occurs in the JKR-model, however, leads to a delay in the detachment process of cells from the substrate compared to the extended Hertz-model (Fig. 5B). The qualitative results in our simulations are very robust against changes of model details (e.g. Ref. 77). Cells may also die by apoptosis before they are pushed out of the uppermost cell layer. However, as long as apoptosis does not affect cells in the proliferating rim the monolayer growth kinetics remains unaffected by apoptosis and as shown in Fig. 1(A).[66]

2.1.3. Co-Cultures

Tumors in-vivo do usually not grow in a liquid environment but in an environment of soft tissue, organs, or at epithelial interfaces. In order to invade the surrounding tissue tumor cells usually release degradative enzymes, notably matrix metalloproteinases and change the expression and localization of certain proteins. E-cadherin, a cell surface adhesion receptor involved in cell-cell contacts, has been found to disappear from cells at the edge of colon carcinoma. Subsequently β-catenin migrates from the cytoplasm to the cell nucleus which leads to an increase of cell proliferation.[73]

The situation of tumor invasion may to some extend be mimicked in co-culture experiments by seeding cell clones in an environment of another cell-type which we briefly illustrate here. A detailed analysis including a sensitivity analysis of different model parameters will be presented elsewhere (Drasdo and Höhme, in preparation). We here focus on the situation before the cell switches to the above described mechanism on for invasion. Our simulations predict that in a co-culture situation a characteristic spatial inhomogeneous pattern may form that is triggered by the proposed form of biomechanical growth inhibition (Fig. 6(B) and (C)). In the simulations a dividing cell clone was initially embedded in a monolayer of non-dividing cells with otherwise the same properties as the dividing cell clone. In our simulations we varied the motility of the embedding cells. If the motility of the embedding, cells is sufficiently large an approximately circular expanding clone forms while for less motile environmental cells an inhomogeneous, finger-shaped structure forms. The finger-shaped structure is a consequence of density

| (A) | (B) | (C) |
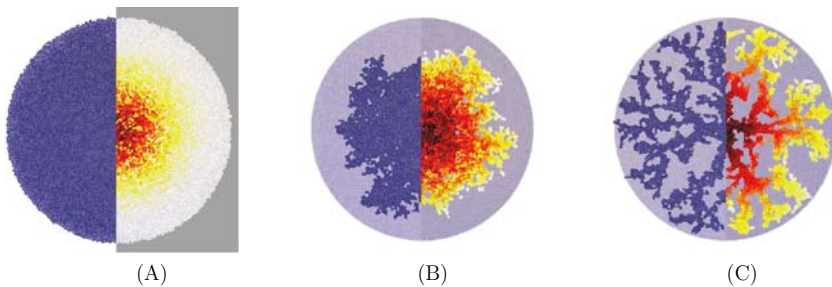
Fig. 6. Morphologies of a monoclone growing as a perfect monolayer in (A) suspension, (B), (C) co-culture. In (B), the motility of the embedding cells (light blue) is twenty times larger than in (C). The colors in the right half of the pictures indicate the proliferative activity; the lighter the cells the shorter is their cycle time. While the morphotype of the expanding clone in (A) is circular, in (B) is compact and largely circular, it is finger-like in (C). Note that in monolayer cultures almost all cells have a good access to glucose. (For the expanding cell clone we here used the JKR-model with the same parameters as in Fig. 5. For the embedding cells we assumed an initial distance of ℓ on a square lattice, no cell-cell adhesion, and $D = 1.27 \times 10^{-11}$ cm^2/s in (B) and $D = 6 \times 10^{-13}$ cm^2/s in (C).)

fluctuations of the embedding cells in that the growing enclosed monoclone forms fingers into the direction where the density of the environmental cells is locally smaller. If the embedding cells are very motile they migrate to escape the outgrowing sprouts. (The situation is expected to be similar if the embedding cells are replaced by granular matter.) Note, however, that at a certain degree of compression, apoptosis may be triggered. In case the embedding cells are more sensitive to pressure and die at a smaller pressure than the growing expanding clone then the growing cells eventually fill the whole space left by the embedding cells.

2.1.4. Border Fluctuations

As shown in Fig. 1, our computer simulations with the off-lattice model were able to explain the growth kinetics ($L(t)$) of the experiments by Bru *et al.*[36] Besides the growth kinetics Bru *et al.* studied the critical boundary properties of expanding monoclones by applying theoretical concepts from non-equilibrium statistical physics used to classify surface growth phenomena into "universality classes." A universality class in homogeneous isotropic interface growth of solids is usually characterized by three critical exponents, the growth exponent β, the roughness exponent α and the dynamic exponent z.[93] The exponents are related by the scaling relation $z = \alpha/\beta$ hence only two exponents are independent and need to be measured. Bru *et al.* suggest that monolayer growth belong to the Molecular-Beam-Epitaxy (MBE) universality class. MBE is characterized by a "raining" or deposition of particles on a surface. The particles then diffuse along the surface. The critical surface dynamics have extensively been studied for Eden clusters which have been proposed as a simple model of tumor growth.[72] The universality class of Eden clusters is believed be the Kadar–Parisi–Zhang (KPZ) universality class (e.g. Refs. 93–95 and Refs. therein), hence Eden clusters do not belong to the MBE universality class. KPZ-growth is characterized by growth along the local normal of the surface which is stabilized by surface tension. For a one-dimensional surface the KPZ-critical exponents are $\alpha = 0.5$, $\beta = 1/3$ and $z = 3/2$ while the MBE-critical exponents are $\alpha = 3/2$, $\beta = 3/8$ and $z = 4$. Usually, the Eden-model has been studied in geometries in which the interface is flat and not circular as for two-dimensional monolayers. In order to systematically study the critical exponents of growing monolayers of circular shape we transfer the growth process onto a random lattice in which a systematic analysis of the critical growth properties including an average over many realizations of the growth process is feasible. We have chosen a random lattice since on regular lattices we have observed lattice artifacts in some parameter regions.[96] In off-lattice models, the too long simulation time does currently not permit a sensitivity analyses over wide parameter ranges or the formation of averages over many realizations of the growth process.

The cellular automaton model is constructed in such a way that it shows the same growth kinetics as the lattice-free approach for expanding monolayers shown in Fig. 1A. In order to avoid simulation artifacts from lattice symmetries we used a Delauney triangulation which can best be understood from its dual graph, a Voronoi tesselation. Assume a random distribution of points in space. Within a Voronoi tesselation to each point that region in space is assigned that is closer to this point that to any other point. The Delauney triangulation results from linking each point to its neighbor points within the Voronoi tesselation. For a random distribution of points the Delauney tesselation is a random lattice with on the average six links to neighbor points. We assume each site on a Delauney lattice can at most be occupied by one cell. The average area which is assigned to a point (= cell) is l^2 which we identify with the average cell area. We start our simulations with a single cell. Cell division is possible only onto free lattice sites. A cell is able to divide if and only if the next free lattice site is available at most $\Delta L / l$ lattice sites away. One interpretation is that a dividing cell is able to exert a sufficiently large force to push at most $\Delta L / l$ cells aside into a certain direction in order to obtain free space for its division. Another interpretation of this rule is that only a limited number of cells can be stimulated to migrate away and leave free space for a dividing cell. It is noteworthy that as $\Delta L \to \infty$ lattice asymmetries in the growth patterns even disappear on a regular (square) lattice; usually $\Delta L / l \sim 2 - 3$ already gives reasonable results.[97] To determine the growth sites we draw a circle of radius $\Delta L / l$ around the dividing cell and shift the neighbor cells of the dividing cell towards the closest free neighbor site within this circle (shifts by more that $\Delta L / l$ lattice positions are prohibited). If a division is permitted we place one of the daughter cells on the site of the mother cell, and the other daughter cell on the neighbor site that has become free as a consequence of the previous shift of neighbor cells. A biological interpretation of the assumption of limited shifts is that a cycling cell stops in one of the cell cycle check points if the division would require a shift of surrounding cells over a distance of more than $\Delta L / l$ cell diameters. As a consequence, the size of the proliferating rim within the expanding monolayer cannot exceed ΔL in case the cells are densely packed (as they are here) which is why we call ΔL the proliferation depth. In the lattice model ΔL it is a free parameter while in the off-lattice model introduced previously ΔL is a consequence of the biomechanical and migration properties of the cells and may for example be influenced by the cell stiffness and motility. Usually, ΔL is larger than the cell diameter $\sim l$. In the classical Eden model,[72] however, $\Delta L = l$ since in this model cells can divide only on empty nearest neighbor sites. The size ΔL of the proliferating rim controls the growth velocity in both, the off-lattice and the cellular automaton model. In computer simulations we found that $\nu \approx \Delta L' / \tau_{\text{eff}}$ with $\tau_{\text{eff}} = \tau / \omega$ being the cell cycle time (results not shown; τ can be measured from the slope of the growth curve in the exponential growth phase as illustrated in Fig. 9C for multi-cellular spheroids). Here $\Delta L' / l \approx [1 + (\Delta L / l - 1)0.685]$

and $\omega = (2^{1/m} - 1)m$. The parameter $m \in [0, 1, 2, \ldots)$ controls the shape (and dispersion) of the cycle time distribution $f(\tau')$. The dispersion of cycle time distribution thereby affects the expansion velocity of the monolayer. We define $f(\tau')$ by

$$f(\tau') = \lambda_m \frac{(\lambda_m \tau')^{m-1}}{(m-1)!} \exp\{-\lambda_m \tau'\}. \tag{7}$$

Here we have chosen $\lambda_m = m$ so that $\langle \tau' \rangle = \tau = 1$ (we refer all times on the intrinsic cycle time τ and set the expectation value $\langle \tau' \rangle$ equal to the intrinsic cycle time). For $m = 1$, $f(\tau')$ is a Poisson distribution and $\omega = 1$. For $m \to \infty$, $f(\tau')$ approaches a δ-distribution peaked at $\tau' = \tau$ and $\omega \to \ln 2$. Hence the larger the dispersion of the cycle time distribution (by choosing m to be smaller) the smaller is ω, and the larger are τ_{eff} and consequently the expansion velocity v of the monolayer. At no dispersion the expansion velocity is the smallest.

The factor 0.685 results from the order in which the cell divisions take place. Although our simulations are in two dimensions, the occurrence of this factor can best be understood if one considers a one-dimensional segment of a two-dimensional growing cell population, ideally a one-cell-thick column ranging from the center of mass of the monolayer until its surface.

If only the outermost cell is able to divide ($\Delta L/l = 1$), the increment within τ is ΔL. However, if the proliferation depth is $\Delta L \gg l$ then the order of divisions determines whether a cell is able to divide or not. To see this assume an almost precise cell cycle length (i.e., a cycle time distribution sharply peaked at $\tau = \langle \tau \rangle$ which is obtained for $m \gg 1$). Then, if it is the innermost cell that divides first then all cells closer to the border are still able to divide while, if it is not the innermost cell that divides first, then the innermost cell cannot divide anymore since this would require to shift more than $\Delta L/l$ cells. So even if $f(\tau') \to \sim \delta(\tau' - \tau)$ the order at which the cells divide matters since for $\Delta L > l$ the cell divisions are not completely synchronous. The factor ~ 0.685 can be calculated from investigating the expected growth increment from all permutations of choosing the cells in the proliferative rim for division. Note that the factor ~ 0.685 marks the difference between an asynchronous and a parallel update. To understand this first note, that since we start each simulation with a single cell, a precise length of the cycle time would mean that all cells divide at the same point of time. The factor ~ 0.685 results from the asynchrony as argued above. For a parallel update this factor would not be expected; the expansion velocity should instead be $v \approx \Delta L/\tau$. (Note that in a circular geometry the expansion velocity may slightly deviate from this value due to the boundary curvature which decreases with increasing monolayer size as $1/r$ with r being the monolayer radius.)

Note also, however, that the factor ~ 0.685 may disappear also in asynchronous updates if the choice of how cells are divided is slightly changed. If one

would assume that a cell that once has passed the restriction point divides with probability one that is, if one assumes the decision on whether a cell divides or not is made immediately after its birth and not when it is chosen for division, then the dependency of the velocity from the order at which the cell divisions in the proliferating rim are performed would no longer be expected.

Next we calculated the roughness exponent α and the dynamic exponent z from the dynamic structure function. The dynamic structure function $S(k, t)$ is defined by

$$S(k, t) = \langle h(k, t)h(-k, t)\rangle, \tag{8}$$

where $h(k, t)$ is the Fourier-transform of the surface height $h(s, t)$ and $\langle \ldots \rangle$ the average over different realizations of the growth process (e.g. Ref. 98). s is here the arclength as in the paper by Bru.[36] To calculate $h(s, t)$ firstly all border cells of the monolayer have to be determined. Then one starts with that cell that has the largest distance from the center of mass (the center of mass is defined by $\bar{r} = (1/N)\sum_{i=1}^{N} \underline{x}_i$ and moves by right turns in counter-clock direction along the monolayer border. $h(s, t)$ is the distance of the border cells from the center of mass. Alternatively we have used the polar angle φ (i.e., studied $h(\varphi, t)$) but did not find noteworthy differences in the simulation results. Here,

$$h(k, t) = \frac{1}{L^{d/2}} \sum_s [h(s, t) - \bar{h}] \exp(iks)\Delta s, \tag{9}$$

where the factor Δs takes into account that the arclength increases with time (otherwise the dynamic structure function-curves do not collapse for different times since in a circular geometry the total arclength increases with time). For self-affine surfaces in absence of any critical length-scale the dynamic structure function $S(k, t)$ has the Family-Vicsek scaling form:[99]

$$S(k, t) = \kappa^{-(2\alpha+1)}\hat{s}(kt^{1/z}), \tag{10}$$

The result shows that $\alpha = 0.5$ (Fig. 7A) and $z = 3/2$ (Fig. 7B) as would be expected for a KPZ behavior and disagrees with MBE.[96] We are currently exploring the effect of fast cell migration on the scaling behavior. However, we like to note that a comment by Buceta and Galeano[100] questions the interpretation of the experimental findings on the dynamic structure function by Bru et al.[36] namely, that the findings indicate a MBE-behavior. We have validated that a small random movement of $\sqrt{\langle(\delta r)^2\rangle} \sim \mathcal{O}(l)$ along the cluster border did not modify the observed exponents[96] (this is the typical distance that a cell travels on the scale of the cycle time in Ref. 55).
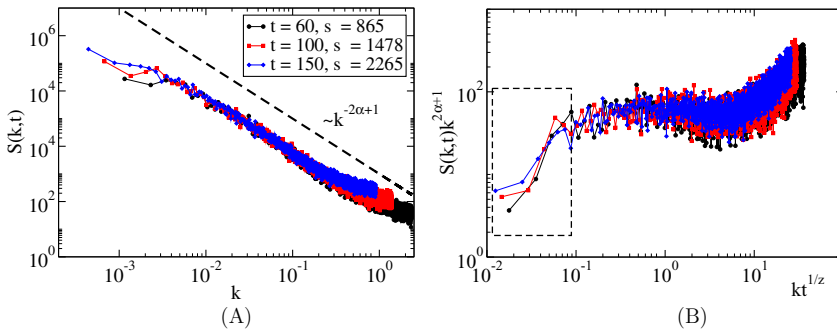
Fig. 7. (A) Dynamic structure function $S(k, t)$ at $t = 60, 100, 120$ (in units of the cycle time $\tau^{(96)}$). The dashed line has a decay of $-(2\alpha + 1) = -2$. This suggests $\alpha = 0.5$ as would be expected from the KPZ universality class. The inset shows the contour of the expanding cell population in a single realization of the growth process. The classification of the universality class furthermore requires to determine either the growth exponent β or the dynamic exponent z. We rescaled the axes due to $S(k, t) \rightarrow S(k, t)k^{2\alpha+1}$ and $k \rightarrow kt^{1/z}$ with the choices $\alpha = 0.5$ and $z = 3/2$ (B). The collapse of the data for small k in the rectangle at $z = 3/2$ is characteristic for KPZ; the growth exponent can then be calculated from the scaling relation $\beta = \alpha/z$ and is $\beta = 1/3$. Note that these results comply with results by Moro[94] obtained with the classical Eden model on a square lattice in $1 + 1$ dimensions in a geometry in which the initial state is a flat interface. The parameters were $m = 1$, $\Delta L = 1$.
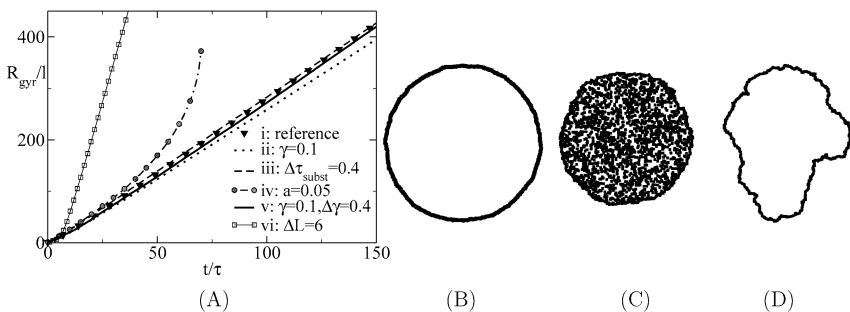
2.1.5. Mutations

So far we assumed that all cells have the same properties and show only stochastic differences for example, in the duration of their cell cycle, the direction of active random migration and the direction of active cell division. We find that the qualitative growth kinetics under these conditions is as depicted in Fig. 1 and insensitive to model details. If cells do not detach from the cell population the initial growth is exponential for the population size and also approximately for the diameter and crosses over into a linear expansion of the diameter and a power-law-like growth $N \propto t^d$ for the population size.

However, aggressive tumors are characterized by their invasiveness which usually were preceded by mutations. Such mutations are known to cause genetic heterogeneity of the cells in a tumor which is subsequently reflected by the heterogeneity of the micrometastases.[49] The capability to invade a surrounding tissue can have many different origins; these include a change of cell-cell and cell-substrate adhesion properties,[101] a change of the migration phenotype[102] or a loss of growth and apoptosis control[18] often, combinations of different changes are involved. For example NIH3T3-HER2 cells are known to suffer from a limitation of cell cycle and apoptosis control;[18] in this cell line an oncogene that encodes HER2/neu, a variant of the HER2-receptor, is expressed. HER2/neu transduces growth-promoting and apoptosis-suppressing signals and have been found in several cancers; different from its normal variant it stimulates proliferation

already at very small extracellular concentrations of the growth factor EGF. Besides invasiveness these mechanisms are able to modify the fraction of proliferating cells and thereby the growth kinetics.

In this subsection we consider the possible effect of mutations that affect the model parameters in the previously introduced cellular automaton model on a Delauney lattice. As an illustration of the potential effect of such a change we consider mutations that with equal probability either increase or decrease the cycle time length by $\Delta\tau/\tau \in [-a, a]$ (Fig. 8). This situation could be given if cells reduce the time they spend in the interphase as a consequence of mutations. However, we found the same qualitative behavior if mutations affect the probability

(A) (B) (C) (D)

Fig. 8. (A) Radius of gyration if mutations occur that affect the length of the cell cycle. The radius of gyration is defined by $R_{\mathrm{gyr}} = \sqrt{(1/N)\sum_{i=1}^{N}(x_i - \bar{x})^2}$ where $\bar{x} = (1/N)\sum_{i=1}^{N} x_i$ denotes the center of mass of the monolayer. If the monolayer forms a perfect disc, $R_{\mathrm{gyr}} = r/\sqrt{2}$ with r being the radius of the monolayer. i: For the reference curve, we assumed $\Delta L/l = 1$, $\gamma = 0$ (no apoptosis), $a = 0$ (no mutations), $\Delta\tau_{\mathrm{subst}} = 0$ (the cycle time is a random Poissonian distributed variable independent of the extracellular environment (substrate)). For the other curves only the parameter that has been changed with respect to the reference curve is given in the legend. ii: $\gamma = 0.1$ (dotted) means that cells die with an apoptosis rate of $0.1/\tau$, iii: $\Delta\tau_{\mathrm{subst}} = 0.4$ (dashed) means that the average cycle time depends on the spatial position of a cell by a value of at most $\Delta\tau_{\mathrm{subst}} = 0.4\,\tau$ (for details, see text). iv: Further we considered mutations in the growth rate $\Delta\tau/\tau$ by at most $a = 0.05$ (dots linked by a dashed line), v: apoptosis with rate $\gamma = 0.1$ (as in (ii)) but with mutations in the apoptosis rate γ of at most 0.4 (full line), and finally, vi: a proliferation layer thickness of $\Delta L/l = 6$. We find that apoptosis reduces the expansion velocity ($\propto d R_{\mathrm{gyr}}/dt$) (see (ii)). If mutations that affect the apoptosis rate occur then the growth curve (see (v)) approaches that without apoptosis (curve (i)) indicating that the apoptosis is down-regulated to zero. In agreement with this observations, mutations that affect the length of the cell cycle time leads to a shortening of the cycle time (see (iv)). A larger size of the proliferating rim increases the expansion velocity (see (vi)). The expansion velocity is unaffected by frozen disorder (see (iii)). (B) shows the proliferation pattern for $\Delta L/l = 6$ ((vi) in (A), the reference case $\Delta L/l = 1$ is used in Fig. 7), (C) shows the proliferation pattern in case of $\gamma = 0.1/\tau$, $\tau_{\mathrm{subst}} = 0.4$ ((v) in (A)). Note that cells proliferate also in the interior to fill the empty places that have emerged due to apoptosis of interior cells. (D) shows the proliferation pattern in case mutations affect the length of the cell cycle ((iv) in (A); simulation with $a = 0.05$; note that here the shape of the population has changed markedly. (In all simulations, $m = 1$.)

of cells to undergo apoptosis. To test this we have seeded one progenitor cell which we assumed to undergo apoptosis with a rate of $\gamma = 0.4/\tau$ and study how γ evolves in the clone if mutations change γ to $\gamma \pm \xi$ (Fig. 8). ξ here is a uniformly distributed random number in $[0, \Delta\gamma]$ with the constraint that $\gamma \in [0, 1/\tau]$ ($\gamma > 1/\tau$ would model a decrease of the total cell population size which should not be considered here). With increasing size of the cell population the apoptosis rate of the border cells decreases revealing the same principle as in the former example: Competition leads to a selection on those properties that eventually lead to an enhancement of the growth of the total cell population. We have also studied the effect of frozen disorder that affect the expected cell cycle time of a cell dependent on its spatial position. The biological motivation was to mimic an inhomogeneous growth environment in which the cell cycle length depends on the absolute position of the cell in space. The underlying assumption was that inhomogeneities of the substrate may affect the cell cycle time according to $\langle \tau'(x, y) \rangle = (1 \pm \xi_{\text{subst}})\langle \tau \rangle$ where $\xi_{\text{subst}} \in [0, \Delta\tau_{\text{subst}}]$ is an uniformly distributed random number. In our simulations this situation does not affect the average growth velocity (Fig. 8).

2.2. Multicellular Spheroids

Tumor cells are often able to grow and divide anchorage-independent. I.e., they can be grown in suspension, not being attached to a substrate, where they form growing spherical aggregates (tumor spheroids). In contrast to monolayers, multicellular spherical aggregates restore morphological and functional features of the original tissue, that is, they possess a three-dimensional network of cell-to-cell and cell-to-matrix interactions with a very similar architecture and function as in vivo.[38] They may contain an extensive extracellular matrix that differs in the relative amount and assembly from the corresponding monolayer cultures. Multicellular spheroids were found to be similar to avascular tumors nodules or microregions of solid in-situ tumors with regard to of the growth kinetics and the spatial structure. Above a certain tumor size of about 400–600 μm they usually consist of proliferating (dividing), quiescent (resting), and necrotic (dead) cells. If the proliferating cells are removed, the quiescent cells re-enter the cell cycle. Cells undergoing necrosis (as opposed to apoptosis[19]) first swell and then undergo lysis i.e. fragmentize into pieces. Subsequently, those cells are usually not considered in the cell count N.

Freyer and Sutherland[103,104] investigated the effect of glucose and oxygen on spheroid growth of EMT6/Ro mouse mammary carcinoma cell spheroids. They reported that during the first 3–4 days the number of cells N grew exponentially fast.[103] After 4 days, N increased only sub-exponentially accompanied by a linear growth of the tumor diameter L (Fig. 9D). Guided by the Gompertz growth law, which is characterized by exponential growth in early stages and saturation at later
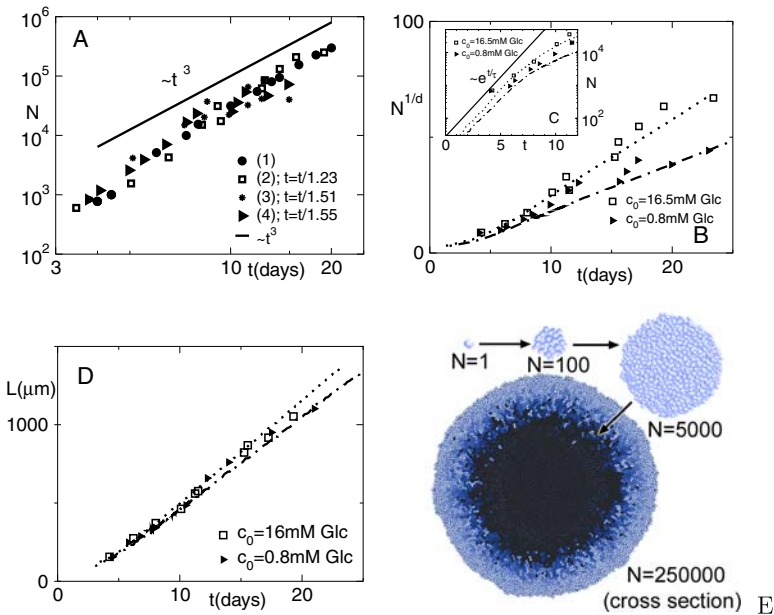
Fig. 9. Tumor growth kinetics. (A) Population size $N(t)$ for tumor spheroids in experiments[103,104] in a log-log plot for different medium glucose c_0 and oxygen o_0 concentrations. (1): c_0, o_0 not known,[103] (2): $c_0 = 16.5$ mM, $o_0 = 0.28$ mM, (3): $c_0 = 16.5$ mM, $o_0 = 0.07$ mM, (4): $c_0 = 0.08$ mM, $o_0 = 0.28$ mM. The time axis for the data (2)–(4) has been rescaled as indicated in the legend to show all data approach a power-law behavior. (B) Computer simulations to the data sets (2), (4) of Fig. 9A (full and dashed-dotted lines). Shown is $N^{1/d}$ vs. t ($d = 3$ for spheroids). (C) Initial growth of population size N for the data sets (2), (4) of Fig. 9A in a lin-log plot (see inset in (B)). (D) Corresponding plots of the tumor diameter L vs. t for the simulations in Fig. 9B. (E) Simulated spatial growth patterns in a multicellular spheroid. Typical tumor growth scenario from $N(t = 0) = 1$ until $N = 250000$ cells in the last picture (shown for a three-dimensional spheroid). The arrows indicate the time direction. Cells in the outer boundary layer (light blue/grey) form a proliferating rim enclosing a layer of quiescent (blue) cells and a necrotic core (black), where glucose has been depleted. If the necrotic cells are removed (as has been done for the computer simulation results in $d = 3$ of Fig. 9B–D), the same pattern as observed experimentally forms. The further parameters were: $l = 18\,\mu$m[103] $T = 22$ h,[104] $E = 300$ Pa,[56,57] $\varrho = 10^{15}$/m^2, $D = 1.5 \times 10^{-12}$ cm^2/s, $\delta = 0.2l$, $\epsilon = \epsilon_s$ (harmonic-like potential energy), $D_{gluc} = 10^{-6}$ cm^2/s,[105] $\gamma_{gluc} = 7.5$–21 mg/(cell h),[106] cells become necrotic if $c(\underline{r}, t) < 7.2 \times 10^{-6}$ mg/mm^3 and apoptotic, if thier cycle time exceeds $3 \times \tau$.

stages, Freyer and Sutherland[103] concluded that the sub-exponential regime of N indicates saturation. In reanalyzing that data we found that plots of $\log(N)$ vs. $\log(t)$ (Fig. 9A) and $N^{1/3}$ vs. t (Fig. 9B) (t denotes time) indicates a power-law-like behavior $N \propto t^3$ rather than a saturation as long as the glucose and oxygen medium concentrations were not too small. This indicates that curve fitting by purely phenomenological growth laws, such as the Gompertz law, can be misleading.

To explore whether the expansion of the tumor spheroid is determined by nutrient limitation as opposed to a biomechanical form of contact inhibition as for monolayers, we use the basic model for monolayer and modify it in some points to fulfill the specific situation of tumor spheroids.

(AMS.1): Within the cell cycle the cell volume increases by a factor of 1.9. The factor of 1.9 accounts for the volume decrease of the cells with the tumor diameter L in multicellular spheroids over the experimental observation period, as observed in Ref. 103 (the assumption that daughter cells are slightly smaller than their mother cell does not affect the main conclusion of this section).

(AMS.2) We here assume glucose to be the limiting nutrient, and that cells can only proliferate if the local glucose concentration $c(\underline{r}, t)$ exceeds a certain threshold. Freyer and Sutherland[104] also studied the growth of multicellular spheroids at varying oxygen concentration. The model for this case would be similar as that for varying glucose concentration which is why we omit it here. For our model of tumor spheroids in suspension we study situations in which a fixed glucose concentration c_0 is maintained outside the tumor. The glucose can diffuse with a rate D_{gluc} and is locally consumed by the cells with a rate γ_{gluc}:

$$\frac{\partial c(\underline{r}, t)}{\partial t} = \sum_i D_{gluc} \frac{\partial^2 c(\underline{r}, t)}{\partial r_i^2} - \gamma_{gluc} \Theta(c(\underline{r}, t)) n(\underline{r}, t) \tag{11}$$

$n(\underline{r}, t)$ is the local density of cells at position $\underline{r}$ and time t. $\Theta(x) = 1$ for $x > 0$ and zero otherwise. We assume that cells become necrotic if the local nutrient concentration $c(\underline{r}, t)$ falls below a threshold. As explained above necrotic cells undergo lysis. We study the case in which lysis is very fast and immediately remove necrotic cells from the simulation (leaving free space at the positions of cells that had become necrotic, so necrotic cells are not considered in the cell count N). We have also checked the case in which we did not remove the dead cells from the core and labeled them as "necrotic" i.e., did not take them into account in calculating the total cell population size of the tumor. For this case we found only a minor difference as a consequence of the pressure that the dead cells in the core exert on the viable rim. However, this difference is very small since cells at the interface between viable rim and necrotic cells cannot divide even if there is free space available since they lack glucose (and oxygen).

(AMS.3) The initial number of cells from which an individual tumor spheroid emerges was estimated from the experiments of Freyer and Sutherland to be $N_0 \approx 30$–100; we start with $N_0 = 1$ and shift the curve along the time-axis until a good fit to the experimental data is obtained.

Figure 9D shows a typical time series of the tumor morphology and snapshots of the layer-like proliferation pattern in tumor spheroids for $N \leq 250000$ cells. The highest proliferation activity is close to the tumor boundary where the local concentration of glucose is the highest, while inside the tumor a necrotic core forms. The

corresponding time developments of the tumor diameter and population size both show a very good agreement with the experimental findings (Fig. 9B–D). After an initially exponential increase of the cell population size (Fig. 9C), $N(t)^{1/3} \propto t$ that is, $N(t) \propto t^3$ for larger times (Fig. 9B). Note, however, that although the spread of the curves for $N^{1/3}(t)$ for the two glucose medium concentrations $c_0 = 0.8$ mM and $c_0 = 16$ mM is significant (Fig. 9B shows that $N^{1/3}(t)$ grows much faster for $c_0 = 16$ mM than for $c_0 = 0.8$ mM) there is almost no spread in the corresponding $L(t)$-curves (Fig. 9D shows that $L(t)$ is approximately the same for $c_0 = 0.8$ mM and $c_0 = 16$ mM). Hence, $L(t)$ is almost unaffected by the 20-fold change of the glucose medium concentration while $N(t)$ is not. Consequently the glucose medium concentration in the range 0.8 mM $\leq c_0 \leq 16$ mM seem to have no influence on the growth of the tumor diameter so the growth of the tumor diameter cannot be determined by glucose control in this case. Since the cell population size does change with increasing nutrient medium concentration, it is the size of the necrotic core (but not that of the tumor) that is controlled by c_0. The only mechanism that in our model can be responsible for the control of the tumor size is the mechanical form of contact inhibition that was already able to explain the existence of the linear growth regime of the monolayers diameter.

Note that since $N \propto t^3$ and $L \propto t$, $N \propto L^3$ despite the (cell-free) necrotic core which seems a contradiction at least for large necrotic core sizes. This pretended contradiction is resolved if one takes into account that the median cell volume v_c decreases with increasing tumor diameter as $v_c \propto 1/L$.[103] This can immediately be seen in case the size ΔL of the viable rim is much smaller than the tumor diameter L; in this case

$$v_c N \propto V = \frac{4}{3}\pi\left(r^3 - r_i^3\right) \approx \pi L^2 \Delta L$$

$$\Leftrightarrow N \propto L^3, \tag{12}$$

where $v_c \propto 1/L$ has been used. Here $r_i = r - \Delta L$ is the inner radius of the viable rim, $r = L/2$ the tumor radius and V is the tumor volume. So interestingly, the decrease of the median cell size and the cell loss due to necrosis in the center of the tumor spheroid occur in such a way, that still $N \propto L^3$ is maintained.

Individual-based models of multi-cellular spheroids have been studied by different authors in recent papers. In Ref. 78 cells are assumed to move deterministically by being pushed by dividing cells. The authors obtain a good agreement of their results with the experimental observations of the population size but unfortunately did not consider the tumor diameter. Lattice-based models of tumor spheroid growth have been considered in Refs. 107–109. Dormann and Deutsch[109] consider a cellular automaton model in which a cell is represented by one lattice site and include the effect of nutrients. Stott *et al.*[108] used a generalized Potts model in which each cell is represented by many lattice sites but did not include the effect

of nutrients. Both models are two-dimensional and in both models the authors compare their findings qualitative with the diameter growth observed in Ref. 110 but did not compare to data on the population size. Jiang *et al.*[107] set up a multi-scale stochastic Monte-Carlo simulation model also based on the generalized Potts model. Each cell occupies up to 64 nodes on a three-dimensional lattice. The authors include an intracellular regulatory Boolean network that controls the G_1-S-phase transition. Their results show a good agreement with the experimental data. The definition of a time scale in their Monte-Carlo simulation is as in Ref. 68, very similar as in this paper. However, they did not adjust their biophysical parameters to experimental observations (for example, the cell-cell and cell-matrix-interaction strengths are taken from simulations about cell-sorting scenarios of Ref. 111 and seem to be markedly too large). Nevertheless the models of tumor spheroids are slowly converging. Off-lattice models as those presented in this paper have the advantage that they permit the use of the same models for cell-cell and cell-matrix interactions as experimentalists do to analyze their measurements on cells (for example,[65]). Lattice models that use many lattice sites to represent an individual cell permit to represent marked changes of the cell shape that may occur in the cause of morphogenetic processes. A major challenge will be to combine the advantages of the off-lattice models with those from the lattice models which use many sub-cellular lattice sites to represent an individual cell. One way to do this may be to consider sub-cellular elements in lattice-free space instead of on the lattice as suggested in Ref. 112. Another major challenge will be to set up a hierarchy of models within a controlled and systematic procedure such that the models on a coarser spatial scale keep that information of the models on a finer spatial scale that is necessary to explain multi-cellular phenomena on the coarser scale.

3. TISSUE SHEETS AND EARLY DEVELOPMENT

For tissue cell sheets which are not attached to an underlying solid, immobile surface and hence can also move in the direction perpendicular to the sheet, the models have to be extended. Many tissue sheets are one-cell-thick. Examples are the intestinal mucosa[48] and intestinal crypts,[46,113] glands,[10] and the blastula of *sea urchin* and *synapta digita*.[43,44] Intestinal crypts are one-cell-thick pockets in the intestinal wall and the cell proliferating machineries responsible for the fast cell turnover of the intestinal wall. After X-ray-irradiation and during adenoma formation crypt fission, i.e. folding of a crypt have been observed. Crypt fission, a process during which one crypt splits into two crypts is also believed to be responsible for the increase of the crypt population.

Finally, during early development in some species a series of cell division from the zygote (the fertilized oocyte) eventually leads to a hollow blastula. At a population size of about 1000 cells gastrulation occurs, an invagination (= inward budding) from which eventually the digestive tract emerges. In all of these tissues the orientation of cell division has to insure that a one-cell-thick-layer is main-

tained. This includes that in case of an increasing population of cells the extra cell mass must be placed into the one-cell-thick layer. If growth and division occur faster than the tissue sheet can be shifted or rearranged to incorporate the extra cells that emerged from the cell division a characteristic fold by a buckling instability can occur. The fold can be initiated by random fluctuations as will be illustrated below for some example. Buckling has separated from the controlled folding that occurs during gastrulation or physiological crypt fission. Budding and buckling can be observed in many tissues such as the lung[8,9] and in the branching pattern of pancreatic cell cultures.[10] In this section we briefly review the Drasdo-Forgacs model[5] originally introduced in Refs. 68, 114 and present additional and new material including precise model parameter definitions that were omitted in the previous publications; the simulation results obtained with this model provide a potential explanation of mechanisms underlying the observed folding patterns of Refs. 8, 10.

3.1. Blastulation and Gastrulation

After fertilization of the oocyte of a deuterostome (this class includes chordates, as human, horse etc, and echinoderms, as sea urchin, sea cucumber, starfish[43]), successive radial *cleavage* (=cell division without cell mass increase) leads to the formation of a hollow spherical blastula composed of a polarized epithelium and enclosing a central cavity, called *blastocoel* (e.g. Ref. 44). The increase in cell number follows an exponential growth law until several thousands of cells have been formed within about one day.[43] Depending on the species considered, the sphere may either be fully symmetric and one cell thick (this is called *radial holoblastic cleavage* and occurs for example in the *sea cucumber Synapta digita*) or possess a lower symmetry. The degree of symmetry is determined by the degree of synchronization of cell division as well as by the orientation of the cell division planes. In the group of animals that show radial holoblastic cleavage, synchronization may either be perfect (as in the *sea cucumber*) or in later stages show differences between the vegetal and animal half as in the *sea urchin*.[43] In the sea urchin it has been shown, that timing and placement of each sea urchin cleavage is independent of preexisting cleavages for the first three cleavages.[115] Two theories have been offered to explain the formation and expansion of a blastocoel. Dan[116] hypothetisized, that the motive force of this expansion is the blastocoel itself. As the blastomeres secrete proteins into the blastocoel, the blastocoel fluid becomes syrupy. This blastocoel sap absorbs large quantities of water by osmosis, thereby swelling and putting pressure on the blastomeres to expand outward. Wolpert and Mercer[117] have proposed, that pressure from the blastocoel is not needed to get this effect. They emphasize the role of differential adhesiveness between the cells and the hyaline layer enclosing them. As long, as the cell remains strongly attached to the hyaline layer, the cells have no alternative but to expand.

Here we study a simple alternative mechanism to blastocoel formation in the case of perfect holoblastic cleavage. Such simulations in three dimensions are still much more time consuming than those of multi-cellular aggregates. Our simulations in this work are therefore two-dimensional, equivalent to considering only spherically (e.g. sea urchin) or axially symmetric (e.g. sea cucumber) embryos. However, drosophila, for example forms a hollow ellipsoid embryo with approximately circular cross-section (since two of the principle axes are equal,[118]) and one axis which is much longer than the other two axes. Thus, all the figures showing cell configurations should be interpreted as two-dimensional projections of three dimensional structures.

Our model is based on the following assumptions:

(B1) cells remain approximately cuboidal during cleavage[43] (i.e. sharp bends of the cell membrane that would result in a large bending energy are disfavored, see Fig. 10). This assumes that cells have a tendency to adopt a spheroidal shape as cells generally do in isolation under culture conditions and that deviations from the spheroidal shape are basically a consequence of the interaction of cells with other cells and the layer they are attached to, see also Fig. 13.

(B2) cell division proceeds at constant embryo mass (Fig. 12A). As observed for example in *sea urchin and synapta digita*[43] each division is oriented
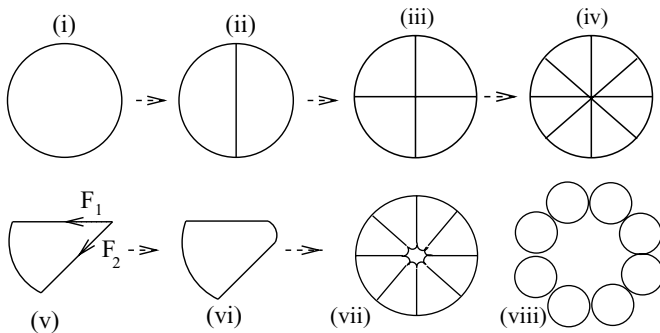
Fig. 10. Schematic sequence of cell divisions (shown in two dimensions) for holoblastic cleavage. (i)–(iv) illustrate an idealized situation with the daughter cells occupying the original volume of the zygote. (v) shows a particular daughter cell from the eight-cell stage. Its membrane, at the periphery and at the center of the cell configuration shown in (iv) has extremely sharp turns. The edges have very high bending energy and, as a consequence, experience a force $\vec{F}_1 + \vec{F}_2$ opposing the curve, as indicated in (vi) (forces are shown only for the center). Depending on the mechanical stiffness of the cell cortex and the bending rigidity of the cell membrane, the rounding of each cell in (iv) results in a cell configuration similar to (vii) (small stiffness), or, (viii) (large bending stiffness). The requirement that a change in cell shape preserves the total cell mass and total cell volume, leads to a net displacement of cell mass away from the center.

in such a way that a one-cell-thick structure is maintained (Fig. 12B). The cell divisions are synchronized, i.e. all cells (or groups of cells) in the developing organism divide at the same time.

(B3) Cells in the early embryo are polar and, as a consequence of the in-homogeneous distribution of their adhesion molecules, form cell-cell contacts in special regions of their membrane, resulting in preferred cell configurations[44] which we believe correspond to local minima in the (free) energy. Deviations from preferred cell shapes and configurations increase the energy. In our model, the energy of a cell configuration contains the following contributions: (i) A nearest-neighbor interaction energy that results from the competition between attractive interactions due to adhesion molecules anchored in the cell membranes, and repulsive contributions from the limited cell deformability and compressibility. For this contribution we assume a similar interaction energy as in the previous Sec. 2 (see Eq. (14)). (ii) A bending energy that takes into account the polarity of the cell layer (Eq. (17)). Cells in a one-cell-thick layer have characteristic apical and basal surfaces. They form contacts with their neighbors along the lateral part. The preferred geometry of the layer and the shape of the cells within the layer depend on the location of cell adhesion molecules as shown schematically in Fig. 11. In the computer model we demarcate an individual cell by a circle that represents the cell in its maximum compressed state. Immediately after the m-th cell division the radius of the circle is $R(m) = R(0)/f(m)$ where $f(m) = \sqrt{2}^m$ to take into account that the total embryo mass (the mass of a cell is identified with the cell area) is constant during cleavage. During cell division, the circle deforms into a dumb-bell at constant area (Fig. 12A). The orientation of the dumb-bell axis is assumed to be optimal if it coincides with the tangent to the local radius of curvature (Fig. 12B). This condition can be translated into the energy contribution which contains an "optimal" angle. For cell i:

$$V_i^{\text{rot}} = \gamma \left(\alpha_i - \alpha_i^{\text{opt}} \right)^2 (\gamma \gg 1). \qquad (13)$$

Here, α_i^{opt} describes the "optimal," α_i the momentary orientation of the cell axis. α_i is optimal if the cell axis is oriented along the tangent to the local radius of curvature i.e. it is constructed in such a way that the daughter cells of a cell for which $\alpha_i = \alpha_{\text{opt}}$ fit well into the tissue sheet (Fig. 12B). For the zygote, the division plane is arbitrary, in the two-cells-state, cells deform in order to form a rectangle after the next cell division. We assume that the elastic properties of the cell layer and the surrounding hyaline layer determine the shape of the nearest-neighbor interaction energy within δ by the parameter ϵ according to the energy
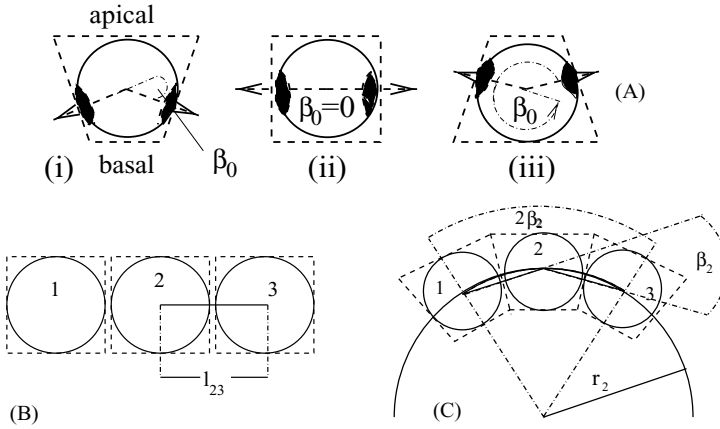
Fig. 11. (a) Preferred individual cell shapes depending on the location of adhesion molecules (black areas). In this two-dimensional representation, the angle β_0 uniquely determines the preferred shape of the cell and therefore the local spontaneous curvature, c_s. Circles with the associated angles demarcate the simplified shape we use to represent cells in the simulations. The optimal configuration of a sheet containing only cells with preferred shapes (i) or (iii) is a closed surface with the basal lamina oriented either towards the interior ((i), $\beta_0 < \pi$), or towards the exterior ((iii), $\beta_0 > \pi$). (b) Preferred cell shape (ii) ($\beta_0 = 0$), results in an optimal configuration with an open, planar cell sheet and equal distance between the centers of (identical) cells. (c) Deviation from the optimal configuration shown in (b). For cell type (ii) any bend (characterized by finite local radius of curvature r and deviation angle β) increases the bending energy. (Here the radius of curvature and the deviation angle is shown only for cell 2.) Note that for cell type (i) the illustrated configuration is optimal if $\beta_j = \beta_0$, where j denotes any cell in the sheet.[68]

contribution

$$
V_{ij}^{NN} = \begin{cases} \epsilon \left(\left[1 + \frac{2d_{ij} - 2\{R_i + R_j\}}{\delta} \right]^2 - 1 \right) : R_i + R_j - \delta \leq d_{ij} \leq R_i + R_j \\ \infty : \text{otherwise.} \end{cases} \quad (14)
$$

Note that $\hat{R} = R - \delta/2$ denotes the radius of a cell in its maximally compressed state. In our two-dimensional simplification we assume that the tissue layer changes its geometry only in the x-y plane while its extension in the z-direction remains $l_z = 50\,\mu\text{m}$ (the size of the zygote of *sea urchin*). Note that we here assumed that contacts between cells are irreversible in contrast to the interaction energy in Eq. (1). (The first line of Eq. (1) can be obtained by setting $\epsilon = \epsilon_s$ in Eq. (14)). The extension of a cell in the x-direction is (see Fig. 13):

$$
l_x = 2R_i + \frac{d_{i,i-1} - R_i - R_{i-1}}{2} + a_i + \frac{d_{i,i+1} - R_i - R_{i+1}}{2}. \quad (15)
$$

a_i is the length of the dumb-bell axis (compare Fig. 12A). For a cell i that adopts its most favored shape within a cell assembly,
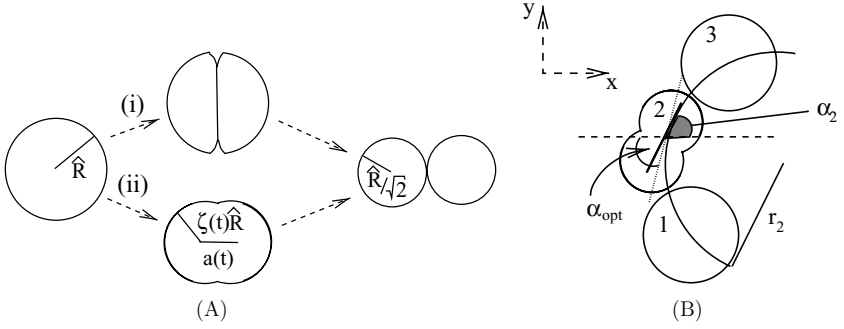
Fig. 12. (A) Cell division in the simulations. We approximate the observed scenario (i) by the scenario (ii). The cell deforms by decreasing its instantaneous radius (in its maximally compressed state) $\hat{R}(t) = \zeta(t)\hat{R}(\zeta(t) < 1)$ from $\hat{R}$(at $t = 0$) $\rightarrow$ $\hat{R}/\sqrt{2}$(at $t = \tau_R$) in small steps ξ, where ξ is a uniformly distributed random number in the interval $0 \leq \xi \leq \xi^{\max}$ with $\xi^{\max} \ll \hat{R}$. The quantity $\zeta(t)$ contains information on the cumulative effect of these small steps. Accordingly, the axis $a(t)$ increases to keep the total area of the cell constant during one division cycle. The dumbbell shape ensures constant area. On a time scale larger than the cell cycle time this choice of the cell division algorithm should not influence the final results. $\hat{R}$ denotes the radius of a cell in its maximally compressed state, which corresponds to the minimal distance d_0 (see Fig. 13) between the centers of neighboring cells (immediately after division) or the centers of the nearest circles of neighboring dumb bells (during cleavage). (B) Determination of the cell division plane in the simulation. The angle α_2 (shaded area) between its axis $a(t)$ (see Fig. 12A) and the x-axis determines the instantaneous orientation of cell 2. In our two-dimensional model this orientation is optimal if $a(t)$ is tangential (denoted by the dotted line) to the local radius of curvature r_2 constructed according to Fig. 12B. The optimal orientation of $a(t)$ defines α_{opt}, the optimal value of α_2 (see text for further details).

$$\frac{d_{i,i-1} - R_i - R_{i-1}}{2} = \frac{d_{i,i+1} - R_i - R_{i+1}}{2} = -\frac{\delta}{4}. \tag{16}$$

hence its size parallel to its axis is $l_x = 2R_i + a_i - \delta/2 = 2\hat{R}_i + a_i + \delta/2$ ($\hat{R}_i$ denotes the radius of cell i in the cells' maximal compressed, R in its relaxed, interaction-free state). Thus, the true size of a circular cell ($a_i = 0$) depends both on R_i, its radius in its maximally compressed state and on the range of cell-cell interactions. Since the cell size shrinks with each cell division, so does δ. After m cell divisions, $\delta(m) = \delta/f(m)$ as $R(m)$. Accordingly, ϵ is also m-dependent (see below).

The polarity of the cells in a one-layered tissue and the stiffness of the layer is modeled by a bending energy according to

$$V^{\mathrm{bend}} = \frac{\kappa}{2} \sum_{i=1}^{N} \left(\frac{1}{r_i} - c_i\right)^2 r_i \beta_i. \tag{17}$$
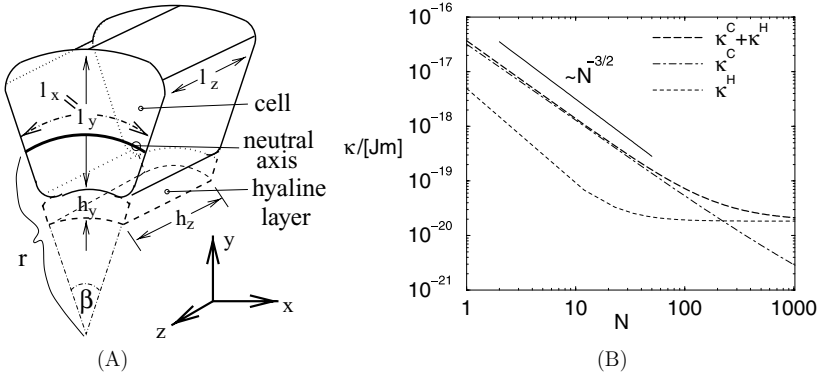
Fig. 13. (A) Sketch of a cell with the hyaline layer. The hyaline layer has a thickness $h_y = 1\,\mu$m. The linear dimensions of the cell in the x, y and z directions are, respectively, l_x, l_y and l_z. Figure 11 shows the projection of the cell onto the x-y plane and defines the quantities r and β. (B) Bending rigidity vs. cell number. The total bending rigidity is the sum of the bending rigidities from the cell layer, κ^C and the hyaline layer, κ^H. For small N, $l_y \gg h_y$ hence κ^C and κ^H are determined by the cell size l_y. $\kappa^C \propto N^{-3/2}$ and $\kappa^H \propto N^{-1}$. For large N, $\kappa^H \to E^H h_z h_y^3 / 12$, $\kappa^C \to 1/\sqrt{N}$.

κ is the bending rigidity, c_s the spontaneous curvature, r_j the local radius of curvature and β_j the local angle of curvature. N is the number of cells at a given point of time. The total energy of a given cell configuration can be summarized to

$$V^{\text{tot}} = \sum_{i<j} V_{ij}^{NN} + \sum_i V_i^{\text{bend}} + \sum_i V_i^{\text{rot}}. \tag{18}$$

ϵ and κ can be expressed in terms of the material properties and the geometry of a cell layer comparing a tissue layer with a continuous, isotropic tissue layer composed of a cell and a hyaline layer (Fig. 13). The parameters ϵ then reads

$$\epsilon = -\left(E^H h_y \frac{l_z}{l_y} + E_\epsilon^C l_z \right) \frac{d^2}{12}. \tag{19}$$

E_H and E_C are the Young moduli of the hyaline layer and the cell layer, respectively. For the definition of the other quantities, see Fig. 13A.

The total tissue-layer bending rigidity is the sum of the bending rigidities for the cell and the hyaline layer,

$$\kappa = \kappa^H + \kappa^C. \tag{20}$$

These are given by

$$\kappa^H = E^H \frac{1}{3} h_z \left(y_0^3 - (y_0 - h_y)^3 \right) \tag{21}$$

$$\kappa^C = E^C \frac{1}{3} l_z ((y_0 - h_y)^3 - (y_0 - h_y - l_y)^3), \qquad (22)$$

where y_0 denotes the neutral axis of the layer,[119] obtained from the condition that in equilibrium the total force on the system consisting of hyaline and cell layer is zero:

$$y_0 = \frac{E^H \frac{h_y^2}{2} + E^C \left(h_y l_y + \frac{l_y^2}{2} \right)}{E^H h_y + E^C l_y}. \qquad (23)$$

As in the previous section on unstructured cell populations we introduced a length, a time and an energy scale and referred all model parameters to groupings of these reference scales in order to obtain a quantitative description on the computer. As the length scale we have chosen the size of the zygote and for the time scale the cycle time τ (=1 h). For the energy scale we again use the "metabolic energy" F_T (here = 10^{-15} J, close to the value in Ref. 59) and for the multicellular dynamics we again use the Metropolis algorithm both as in Sec. 2. The method has been compared to direct integration of stochastic over-damped equations of motion for related biological problems as those presented here and have been found to work well as long as the noise influence is not too small compared to directed forces and provided, the step sizes for migration and orientation changes are chosen sufficiently small in order to insure a linear velocity-force relation. If the deterministic forces exerted on a cell are much larger than the random forces that represent the active random component of cell movement, however, equations of motion are more appropriate (see for example Refs. 47, 78, 120, 121). Different from Sec. 2 we assume in most of the simulations shown below that the growth step size $\delta a \in [0, \delta a_{\max}(m))$ and the migration step size $\xi \in [0, \xi_{\max}(m))$ depend on the cell size (indicated by m, the number of divisions a cell has performed). The m-dependencies of the maximum growth and migration step sizes are determined by the requirements that (i) the cycle time is independent of the cell size and (ii) the diffusion constant scales as the inverse of the cell size. However, the qualitative behavior does not change if the latter assumption is dropped.[114] The simulation is performed as explained in Sec. 2 (compare also Appendix A for further details). Figure 14 shows a typical simulation run. We started our simulations with a single zygote and stopped it at the 1024 cells-stage. The zygote divides a number of times until the embryo becomes a circle, the 2-D analog to a one-cell-thick hollow blastula. The cell population grows exponentially as observed in experiments[43] and the perimeter U develops with $U \propto \sqrt{N} = \sqrt{2^{t/\tau}}$ (Fig. 15). We predict that in the three dimensional-analog the growth of the blastula diameter should be $U \propto 2^{t/(6\tau)}$ which results from a small calculation. This may well be tested in synapta digita since in this animal all cells are of equal size at a given point of time until $N > 1000$ (in contrast to sea urchin, where cells of the animal pole perform more cell divisions than those of the vegetal pole). Above a certain size
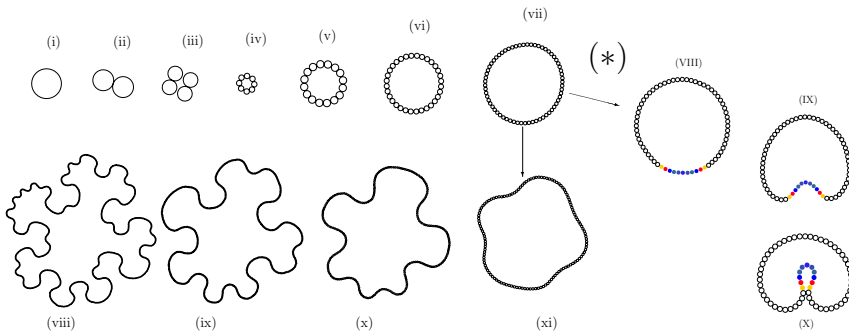
Fig. 14. The evolution of the cellular pattern in the computer simulation for $\epsilon(0) = 5 \times 10^{-14}$ J and $\kappa(0) = 3.5 \times 10^{-16}$ Jm. As explained in the text the magnitudes of these parameters vary with the size of the cells, i.e. with the number of cell divisions, m. The above values refer to the zygote ($m = 0$). For the chosen values of ϵ and κ configurations (i)–(vii) correspond to normal development. A dynamical instability sets in after the 64-cell stage (vii), which in a spherical embryo would correspond to about 2000 cells. (Due to the uncertainties in the experimental values of $\epsilon(0)$ and $\kappa(0)$, such an instability would not necessarily occur at the 2000 cell stage.) With further growth of the cell population the folding of the blastula becomes more pronounced, as seen in patterns (viii)–(xi). The observed scenario that follows configuration (vii) is an invagination as shown in (VIII)–(X) (denoted by "*"). At stage (VIII) 11 cells are assumed to change their cytoskeleton in such a way that the spontaneous curvature locally becomes negative. From the leftmost cell 1 to the rightmost cell 11 the spontaneous curvatures follow the pattern $c_1, c_2, c_3, c_4, c_5, c_6, c_5, c_4, c_3, c_2, c_1$, with $c_i = \Delta \times i$ (i.e. cells 1 and 11, 2 and 10, etc. have pairwise the same spontaneous curvatures). Here, $\Delta = -2$. Note that the all cells change shape simultaneously in the whole invagination region as pointed out by Refs. 118, 122. (X) shows the developed gastrula stage.
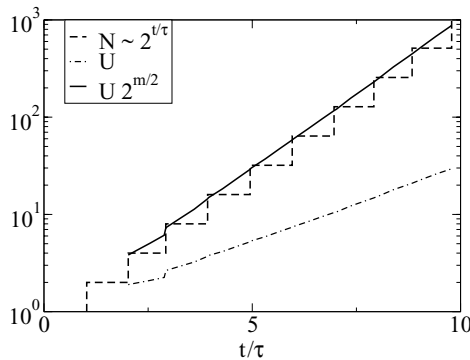
Fig. 15. The cell population size N and the perimeter U vs. time for the parameters of Fig. 14(i)–(xi). $m = t/\tau$ is the number of division cycles the zygote has performed. $N = 2^m$ and for the perimeter $U \propto \sqrt{N}$ (the equivalent relation in $d = 3$ would be $U \propto N^{1/3}$). Note that $N \propto 2^{t/\tau}$ as experimentally observed[43] and note the step-like increase of the cell population size that occurs as a consequence of the synchronization of cell division.

of about ∼64 cells in $d = 2$ the circle (blastula) becomes unstable and buckles (Fig. 14(viii)–(x)). At the onset of buckling the stabilizing forces (here: bending forces) are no longer large enough to balance the de-stabilizing forces that emerge as a consequence of cell division. Small stochastic fluctuations are sufficient to cause small undulations of the blastula cell layer that are enhanced by cell divisions. Hence eventually the layer buckles and forms spatial patterns as those presented in Fig. 14(viii)–(x). The existence of the buckling does not depend on the choice of the parameters, only the size of the blastula at which it occurs does. Below we study the onset of the instability in some more detail. Such a buckling instability would derail normal development and hence it must be suppressed during morphogenesis. At about 1000 cells corresponding to about 50 cells along the perimeter of in the two-dimensional circular cut of the blastula cell division stops and an inward budding (gastrulation) occurs. From this invagination later the digestive tract emerges. We model the invagination by assuming a differentiation takes place in a small "contractile region" which changes the spontaneous curvature to negative values $c_s < 0$ (Fig. 14(VII)–(IX)). This is motivated by experimental observations of a simultaneous movement of the cell nuclei from the outer (apical) towards the inner (basal) cell membrane resulting in an active shape change of cells and macroscopically in an invagination.[122] In the simulations of Fig. 14 we assumed that c_s decreases from the border of the invaginating region with a gradient of c_s towards the center of the invaginating region; for constant c_s the invaginating region has a more circular cross-section and deviates from the approximately tube-like shape that has been experimentally observed in sea urchin (Fig. 16; Ref. 43). For the parameters chosen in our simulations the size of the circle at the instability corresponds well to the size of a 2d-section of the blastula at the stage where gastrulation sets in. The change of the spontaneous curvature locally increases the energy (Fig. 16). The relaxation of the energy then provides the driving force the invagination. Buckling, on the other hand, increases the configuration energy.

3.2. Generic Behavior of Buckling

In the morphogenetic and tissue maintenance processes of one-layered tissues that follow blastulation neither a cell mass conservation nor a strict synchronization of cell division is found. Examples are buckling in embryonic lung tissue[9] and the branching pattern of pancreatic cell cultures.[10] In these patterns labeling experiments show that cell proliferation is larger in regions of larger curvature. In order to test whether our model can explain such labeling pattern we ran equivalent simulations as those for blastulation firstly dropping the assumption of the total cell mass be constant. The result (Fig. 17) clearly illustrates that buckling does not depend on the presence of synchronization. Moreover cells in regions of larger local curvature are found to be smaller than cells in regions of smaller local curvature.

This occurs since cells in regions of larger local curvature have performed more divisions than cells at regions of smaller local curvature (and hence are
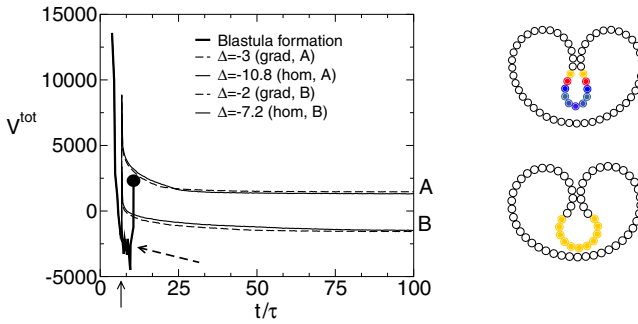
Fig. 16. Total configuration energy of the cells at the transition from a blastula to a gastrula after a differentiation of cells that results in a change of the cell shape. Immediately after the differentiation that leads to a negative spontaneous curvature (arrow at the x-axis), the mechanical energy increases and presents the driving force for the invagination. We compare simulations where all cells within the invaginating region have the same spontaneous curvature with a situation where the cell in the middle of the invaginating region has the largest negative spontaneous curvature increasing towards the border of the region by an increment of Δ. The curves A,B represent simulations where the energy in the invaginated state is different. The energy value for the blastula without invagination represents the stage (xi) in Fig. 14; note that at the point where the buckling instability occurs (denoted by an arrow at the x-axis), the energy rapidly increases (the big black dot denotes the termination of the computer simulation for this case). As illustrated by the two figures for curve A on the right, the invagination pattern is more tube-like if c_s changes gradually (upper picture) compared to the case of constant c_s that generates a circular cross-section of the invaginated region (lower picture). Eventually the cell configuration relaxes into a new equilibrium. Generally, the smaller c_s the more pronounced is the invagination and the larger is the energy in the minimum free energy state (curve A with a gradual change in the spontaneous curvature corresponds to the invaginated state (X) in Fig. 14).

smaller due to the used cell division algorithm in Fig. 12A), in agreement with the experiments that have shown that the cell proliferation activity is larger in regions with large bends.[8,9]

Next we dropped the assumption that the total cell mass be constant using the division algorithm sketched in Fig. 2A and again found the same type of buckling instability (Fig. 18). For large κ and τ a buckling occurs in the power-law growth regime (indicated by an upwards bend in the growth curve of Fig. 18(C and D)).

However, as seen for gastrulation, a reliable invagination requires a differentiation that changes locally the properties of the cells. Alternatively to a locally negative curvature, one may think of a line tension which would occur if neighboring cells of different types are disfavored to form cell-cell contacts (Fig. 19). In this case, however, the pre-bend structure determines whether an inward budding or an outward budding occurs; the minimum free energy configuration may again not be attainable. Such mechanisms could be involved in the fission of intestinal crypts either in the large or small intestine.[45,123,124]

(A)   (C)   (E)

(B)   (D)   (F)
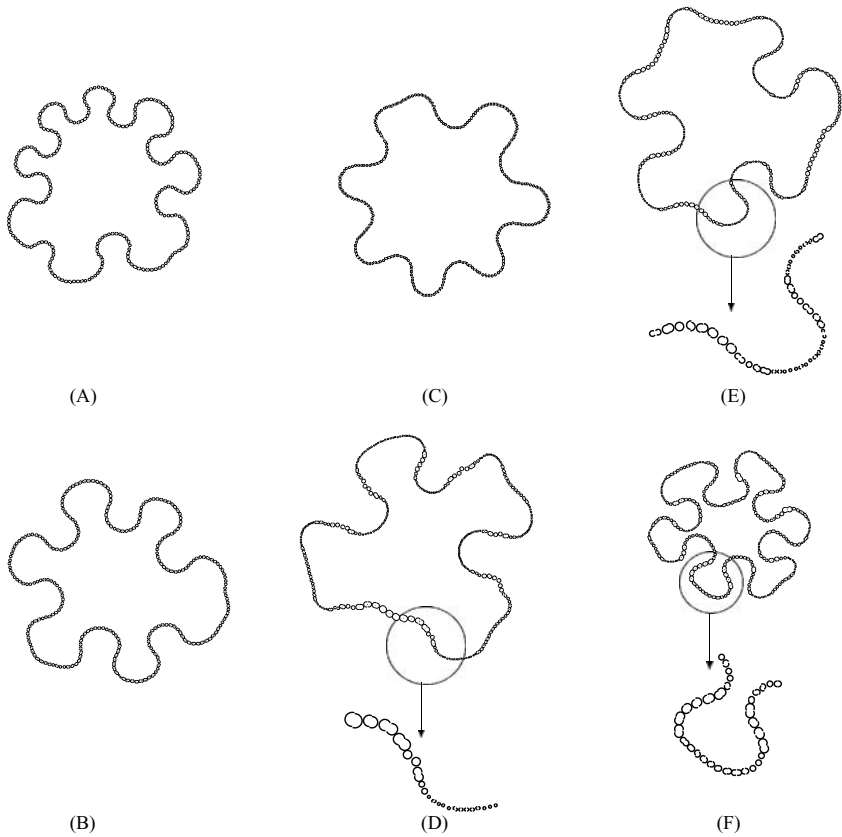
Fig. 17. Folding patterns at $N = 512$ cells at constant embryo mass if synchronization is dropped. (In order to study the possible spectrum of behavior we here and in the following figures vary κ and ϵ independently; such a behavior can be obtained by anisotropic material properties of the cell layer and proper migration parameters.) The configurations in the top line are still growing exponentially and in the bottom line according to a sub-exponential growth law. The picture pairs (A) and (D) differ only by the ϵ-value, (B) and (E) by the bending rigidity, (C) and (F) by the cell division rate. (In particular: (A) $\tau = \tau_0/2, \kappa = 300, \epsilon = 2000$, (D) $\tau = \tau_0/2, \kappa = 300, \epsilon = 20$, (B) $\tau = \tau_0/2, \kappa = 100$, $\epsilon = 200$, (E) $\tau = \tau_0/2, \kappa = 1000, \epsilon = 200$, (C) $\tau = 5\tau_0, \kappa = 300, \epsilon = 200$, (F) $\tau = 0.05\tau_0, \kappa = 300$, $\epsilon = 200$). The snapshots (A), (B) and (C), all taken from exponentially growing cell configurations are very similar, in these cases the thickness of the cell chains is homogeneous over the configurations. Different from that, in (D), (E) and (F) the cells at strong bends appear thinner than those at small bends. (D) and (E) indicates that small ϵ have the same effect on the cell configuration as large κ values: the ratio ϵ/κ determines if the contribution of the interaction energy or the contribution due to bending is more important. (F): large growth rates drive the system far from equilibrium (the equilibrium state is a perfect circle).
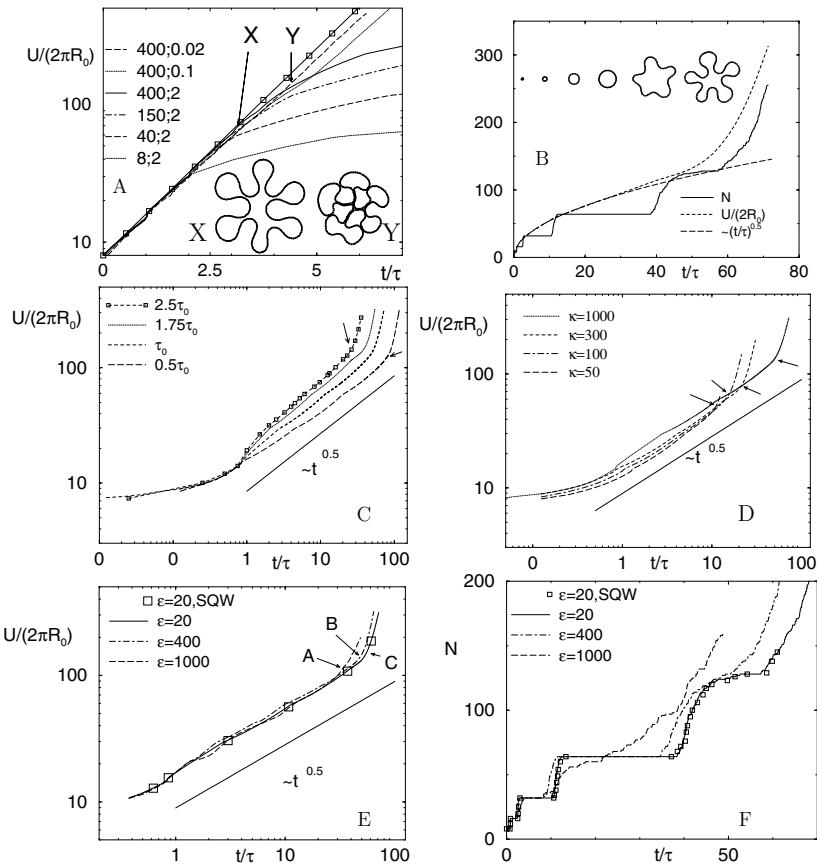
Fig. 18. (A) Number of cells N vs. time t/τ for growing closed 1d multi-cellular manifolds in the absence of synchronization and if the total mass of the cell configuration is not conserved (i.e. using the division algorithm of Fig. 2A); the first row in the legend denotes τ/τ_0 (here, τ_0 is a reference cycle time), the second row $\kappa/10^3$. For very large cycle times τ (or equivalently, a very large cell motility) the closed one-dimensional cell manifolds again grow exponentially fast. (B) N and perimeter U vs. t for $\tau = \tau_0$, $\kappa = 1000$ and $\epsilon = 10$ without explicit synchronization of cell division and the corresponding cell configurations at $N = 8, 16, 32, 64, 128, 256$ cells. The cells divide nearly synchronously as long as the configuration corresponds to a perfect circle. With increasing deviation from a perfect circle, the synchronization breaks down. Note that for small τ (or equivalently, a small cell motility) the growth of the circular (hollow) multicellular geometry is no longer exponentially fast but as $U \propto \sqrt{t}$ (C,D). (C): $U/(2\pi R_0)$ ($R_0 = R + \delta/4$) vs. t for different choices of τ in a regime where τ is small and (D) different choices of κ. In all simulations, $\epsilon = 20$. The arrows in (C), (D) indicate the points where an instability occurs; the smaller are τ and κ, the earlier the instability occurs. (E) We have also varied ϵ: the larger ϵ is, the smaller is the domain size at which a bucking occurs. (F) shows the corresponding diagram of N vs. t; the earlier the instability occurs earlier a de-synchronization of cell division sets in. (In (E,F) we added a curve with a simple square-well potential illustrating the robustness of the results.)
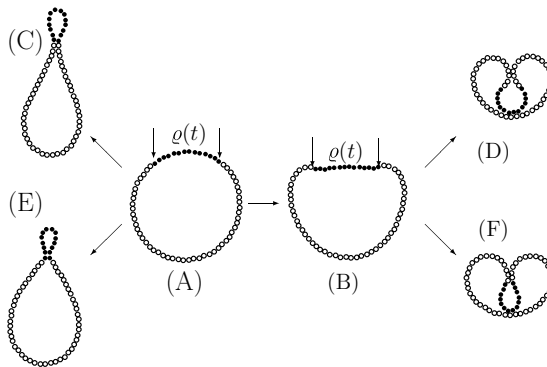
Fig. 19. Reliable folding requires either an active cell shape change or may be driven by a line tension. (A) start configuration after the differentiation. The ($N_A = 14$) cells of type A (black) have different physical properties than the ($N_B = 50$) white ones of type B. Differential adhesiveness between the A-cells and the B-cells may result in an edge energy $E^{\text{edge}} = \sigma \varrho$ where ϱ denotes the linear size of the patch of region A. (B) To obtain an invagination as shown in (D) and (F), the cells have to pass over configuration (B), where the region of A-cells is stretched and thus ϱ as well as the edge energy E^{edge} has a maximum. (C) shows the equilibrium configuration for $c_0^A = c_0^B = 0$ and $\sigma = 4 \times 10^5$. In order to minimize the edge energy the system shows budding, but different from a system with negative spontaneous curvature, outward not inward budding. (D) Perfect invagination obtained for $r_A \approx c_0^A = -1/43$, $r_B \approx c_0^B = 1/12$. (E) If the system has a line tension and a negative spontaneous curvature ($c_0^A = -1/43$, $c_0^B = 1/12$ and $\sigma = 4 \times 10^5$), despite the fact that the global energy maximum is an inward bud (F), the system buds outward into a local energy minimum. The reason for this is a kinetic one: each system invaginating has to pass configuration (B) which for large σ requires a too large activation energy. (F) configuration of minimum energy for ($c_0^A = -1/43$, $c_0^B = 1/12$ and $\sigma = 4 \times 10^5$), calculated by "switching on" the edge energy after configuration (B) has been passed. Different from (D) where $\sigma = 0$, the edge length is smaller causing the invaginated bud to be smaller as well.

The results of the simulations for both, multi-cellular aggregates (monolayers and multi-cellular spheroids) and tissue layers are remarkably robust. A change of the potential energy from harmonic to the Hertzian or the JKR-model (Fig. 2C; and for some cases even square-well, see Fig. 18(E) and(F)), a replacement of the combination of the isotropic potential cell-cell interaction energy and the bending energy by a polar potential energy shown in Fig. 20, or the use of overdamped equations of motion (of the type outlined in Eq. (6)) for each cell instead of the Metropolis algorithm that was used here did not change the results for the selected cases we looked at.

4. DISCUSSION

Recent experimental findings, often complemented by a comparison to results of mathematical models suggest that mechanical interactions play an impor-
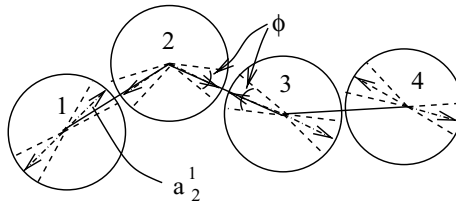
Fig. 20. Instead of a bending energy in combination with a homogeneous cell-cell adhesion potential to model the cell polarity we have also used a direct approach with a polar cell-cell adhesion energy. There we assumed a small contact region (denoted by the symbol Φ); adhesion is only present if the contact regions of neighbor cells overlap (which is the case for cells 1, 2 and 2, 3 but not for cells 3, 4). Contacts in which the connecting line between neighbor cells separates the contact region in two equally large segments (as, for example for cells 2, 3) are favored. After each cell division contacts were assumed to be re-organized. The qualitative results were as those for the bending energy.
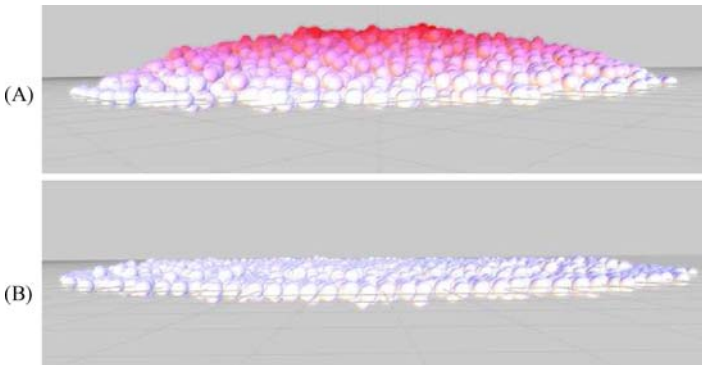
Fig. 21. (A) If the cell-substrate adhesion is not strong enough to prevent cells from being pushed out of the monolayer, cells pile up in the absence of anoikis. The intensity of the red color denotes the distance to the substrate. Here we assumed that cells can re-enter into the cell cycle if the stress is relaxed and their degree of compression falls below a critical threshold. (B) If the interior cells can actively relax stress by down-regulating the stiffness of their cytoskeleton (here, we assumed that the Young modulus changed from $E = 450\,\text{Pa} \rightarrow E = 200\,\text{Pa}$) then the interior cells relax stress and almost all stay in the monolayer.

tant role in growth and pattern formation phenomena of multi-cellular systems. Examples are multi-cellular spheroids embedded in agarose gel,[6] cell monolayers growing on properly dissected surfaces faces[7] and imaginal disc growth.[11] Based on previous findings in growing monolayers of tumor cells in-vitro and recent results of in-vivo situations Bru *et al.*[125] have speculated that after stimulation of a immune response neutrophils may stop tumor expansion mainly as a consequence of the competition of cells for free space. We have demonstrated by computer simulations based in individual-cell based models that the observed growth kinetics in both, monolayers and multi-cellular spheroids may largely be explained by

a biomechanical form of contact inhibition. Our simulations were based on the assumptions that a growth stop maybe triggered by a certain degree of deformation or compression. Without a mechanism that controls a growth stop, a perfect monolayer would never form but cells would be pushed out of the monolayer if the stress generated by the growth would overcome a certain threshold value that is given by the strength of cell-substrate adhesion. We here focused on compact cell aggregates; some monolayer phenotypes in particular fibroblasts show initially a sparse distribution of cells; however, it may be argued that their expansion is expected to qualitatively follow a Fisher–Kolmogorov–Petrovskii–Piskounov (FKPP)-equation-like dynamics such that these eventually again form dense aggregates.[97] Recent findings suggest that cells are able to regulate their properties such that stress within monolayers is relaxed.[7] Figure 21 shows that down-regulation of the cytoskeleton stiffness of interior cells at a critical stress is able to stabilize a quasi-monolayer even in case the contact inhibition is not sufficient to prevent cells from being pushed out of the monolayer. Cells that experience larger deformation or compression on average have a longer cell cycle length than cells which experiences less deformation or compression; isolated cells are assumed to have the smallest (average) cell cycle length. We suggested to test our proposed mechanism either by tracking the fate of individually labeled cells which we predict form clones of largely varying sizes even in case they emerged at almost the same time during the growth process, or in co-cultures of cells growing in an environment of non-dividing cells where we predict that the spatial pattern depends largely on the physical properties of the embedding medium. For example, if the cells that enclose an expanding clone have a large motility the geometric shape of the expanding clone should be more compact while in case the motility of the environmental cells is small, finger-like growth patterns should form. Finger-like growth patterns can also be triggered by a large adhesion between the environmental cells; in this case the environmental cells adhere in small patches leaving free space between the patches for the growing cell clone to expand (Drasdo and Hoehme, in preparation). We expect that the same qualitative growth scenario would be found if instead of cells colloidal particles would be used as an embedding medium. Such experiments would be a natural extension of the experiments by Jain and co-workers.[6,126,127] Interestingly, random fluctuations in the cell cycle length result in a larger growth velocity of a cell population compared to cell populations where cell division occurs synchronized even in case the expectation value of the cell cycle length is the same.[97] This phenomenon may be an explanation for the observation that Glasgow osteosarcoma in mice grow faster if the circadian rhythm, that regulates the synchronization of cell division in the intestine, are suppressed.[128]

Mutations are known to affect the control of apoptosis and of the cell cycle.[18] How is a tumor expected to evolve in case the apoptosis is increasingly down-regulated or the length of the (or passage into the) cell cycle is increasingly upregulated? Our simulations for this case suggest that a selection on cells

which show a faster passage through the cell cycle occurs i.e., a selection on cells that grow and divide faster and undergo less apoptosis. This modifies the shape of the growth curve qualitatively since it generates a drift of the average effective cell cycle length (or in other words, growth time) towards smaller values. Hence random mutations here are a source of diversity of properties which-by selection-eventually leads to an overall increase of the growth velocity of the cell population.

The microscopic processes of growing tumor interfaces can be concluded to a large extend from the critical exponents that characterize the fluctuations of the interface. Bru et al.[36] suggested that the growth pattern in tumor mono-layers belong to the Molecular Beam Epitaxy class. Buceta and Galeano[100] question this. We have performed simulations in 2d-monolayers which clearly suggest a KPZ-like behavior; however, in our simulations the hopping was ne-glected or chosen to be of the order of the cell diameter; however, very recent simulations with a larger hopping rate indicate that the surface dynamics remains KPZ-like.[96]

As a second example we studied the stability of growing tissue layers that are not attached to a fixed surface (as opposed to monolayers that grow on a flat fixed substrate in a petri dish). An example for this situation is the blastula formation of species that form a one cell thick hollow blastula (geometrically a hollow sphere). Here, the one-cell-thick layer is stabilized by mechanical energy. Starting from a model introduced in Ref. 68 we have shown that buckling oc-curs if the stress generated by the growing and dividing cells can no longer be balanced by the stabilizing mechanical energy (here, the bending energy; sim-ilar effects can be observed for expanding elastic shells if shear stress plays a role[129]). The origin of the layer-stabilizing mechanical energy is the cell polarity. This differs from monolayers growing on fixed substrates in that a piling up of cells rather than a buckling occurs if the monolayer gets unstable. We have shown examples that clearly suggest that the emergence of buckling does not depend on specific mechanisms that are observed in blastula formation such as a syn-chronized cell division or a conservation of the total embryo mass but that this effect is generic. This line of argument is supported by observations for example in lung[9] and pancreatic cells[10] which show that cell division is stronger at po-sitions of larger local curvature; this is precisely the result that we found in our simulations.

Hence, in summary, many experimental observations in multicellular systems can be explained by assuming cells are simple physical particles, performing (active) random moves and moving under the influence of external forces, and being able to grow and divide. Such a dynamics may be modeled by a master equation (e.g. Refs. 66, 69) or a system of Langevin equations.[77,120]

By comparison of the model results with experimental findings it is largely possible to identify at which point in a growth or pattern formation process reg-
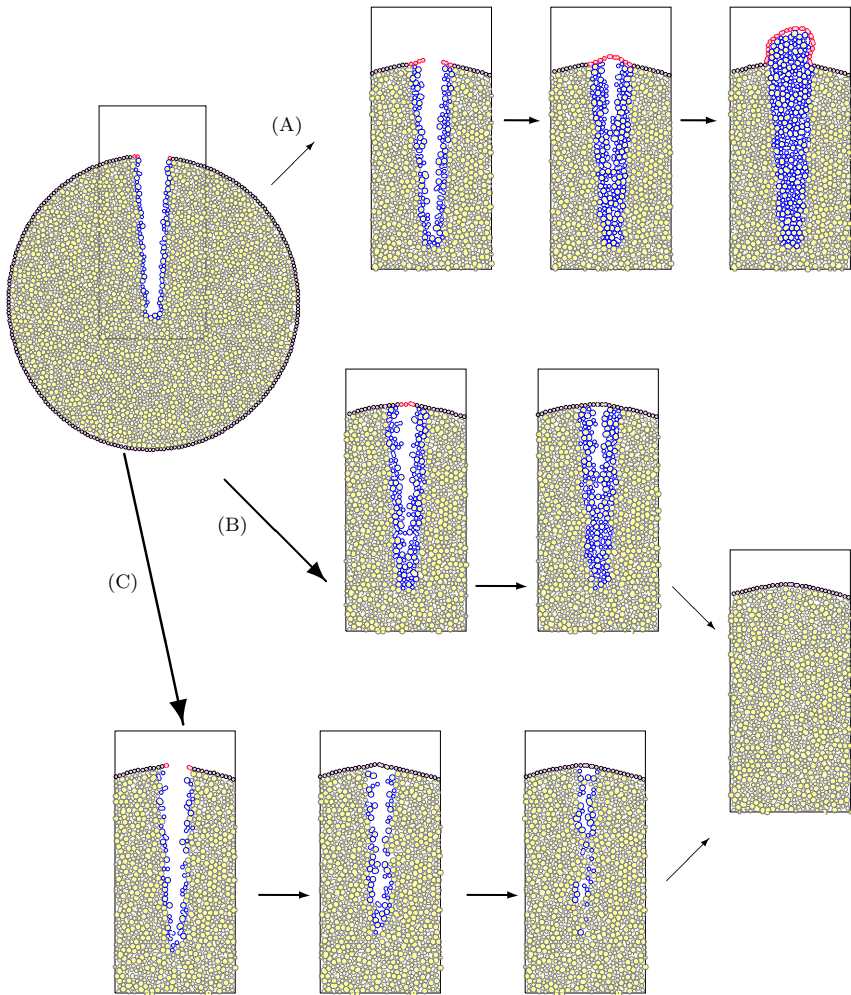
Fig. 22. Highly simplified sketch of a simulated regeneration scenario after a cut-like lesion of a two-dimensional model tissue (skin), composed of epithelial cells that represent the key component of the epidermis and fibroblasts representing an important component of the dermis. The dermis is located below the epidermis and consists of the papillary and reticular dermis. The papillary dermis is directly located below the epidermis and has a high density of fibroblasts while the reticular dermis is a loose connected tissue with a much lower density of fibroblasts. A scar is often accompanied by an over-production of soft tissue (hypertrophic scars, kelloids) which then leads to a local protrusion of the skin. Within our model, in the initial configuration, cells at the surface of the lesion are switched into the proliferating state as is known from observation.[130] Epithelia are marked pink, with black (quiescent) or red (prolif.) boundaries. They are assumed to grow by directed cell division and to form polar contacts to their neighbors at their side membranes. Fibroblasts are drawn in yellow, with grey (quiescent) or blue (prolif.) boundaries. (Usually the fibroblast density is smaller than in the picture.

ulatory or genetic changes of cells or groups of cells must have occurred. At this point the simulated (model) scenario deviates from the one that is experimentally observed. Examples for this are the growth stop of monolayers at confluence observed for many cell lines and gastrulation, i.e. the invagination that occurs prior to the potential occurrence of a (buckling) instability in early development.

Noise is inherently present in biological systems. We have shown that it can be the source for instabilities and even modify the expansion velocity of growing multicellular aggregates. Moreover, as explained above the fluctuation structure of the interface between an expanding cell clone and its environment may permit to conclude the migration and growth behavior on the single-cell level. However, significant qualitative differences in the system behavior of cell populations where found in our simulations only in case of random mutations that affect the cell-biological properties of the cells (in our case the apoptosis or growth control).

Still, most models are not at a level where they permit quantitative predictions. However, the advance in experimental techniques increasingly permit to study the effect of molecular changes on the multi-cellular phenotype of tissues and tumors. This requires to spatially and temporally resolve the intracellular regulatory mechanisms. Some attempts into the direction of multi-cellular models that include an internal structure has been made recently in the context of development and morphogenesis (e.g. Refs. 35, 131, 132) and in the context of tumor growth (e.g. Refs. 107, 133). Studies along this line, performed in close contact with experiments, will eventually permit to improve the models such that they can be used for analysis and predictions in biotechnological applications,[134,135] cancer treatment (e.g. Refs. 136–139), and regenerative medicine (see Fig. 22 for a sketch of the regeneration of a cut-like region; examples where single-cell based models are a proper choice compared to continuum mechanical models are epithelial regeneration processes as in skin[140] or in liver after toxification[141] or partial hepatectomy[142]).

Fig. 22. Continued. One may interpret the yellow elastic circles also as soft tissue composed of both, extracellular components and fibroblasts.) The scenario A–C show different mechanisms how the lesion could be closed. In order to prevent budding (shown in (A)) which would occur in the absence of a growth stop, a correct closure of the lesion as in (B),(C) requires an an active switch from prolif. → quiescent. Scenario (B) leads to a gradual differentiation of fibroblasts by signals from their nearest neighbors (since cells at the inner border of the lesion drawn in blue have less neighbors they continue to proliferate until the lesion has been closed). In (C) a transition from prolif → quiescent for fibroblasts occurs as a consequence of a too large compression of the cells. Epithelial cells stop growing if they come into contact at their side membranes: this also models a biomechanical form of growth stop.

APPENDIX A: TIME SCALES AND STEP SIZES IN
THE MONTE CARLO SIMULATION

Each growth trial that doesn't result in an forbidden large compression of a cell (i.e. $d_{ij} < R_i + R_j - \delta$ which denote excluded volume (EV) interactions) is accepted. The cycle time of a cell not subject to EV interactions after m divisions is

$$\tau = \frac{2R(m+1)n_g \Delta t}{\overline{\delta a}(m+1)} \tag{A.1}$$

where $\overline{\delta a}(m) = \delta a_{\max}(m)/2$ is the average growth step size, n_g is the number of migration trials between two successive growth trials, $R(m)$ is the cell radius after the cell has performed m divisions, Δt the time interval between two successive migration trials and $n_g \Delta t$ the time between two successive growth trials. In the monolayer simulations, the cell size is independent of the number of divisions a cell has performed so $R(m)$ and $\delta a_{\max}(m)$ do not depend on m. In the tumor spheroid simulations and in the blastula formation simulations, however, the cell size decreases with m. Equation (A.1) should express that in the absence of external influences the number of growth steps between two successive divisions which determine the cell cycle length has to be invariant under a change of the cell size. Consider a zygote (here: $m = 0$, and the radius of the zygote is $R(0)$). Then in passing from the zygote to the two-cells stage, $\tau = 4R(1)n_g \Delta t/\delta a_{\max}(1)$ should be the same as in passing from size $R(m)$ to $R(m+1)$, given by Eq. (A.1). $R(m) = (R(0)/\sqrt{2^m}$ and $\delta a_{\max}(m) = \delta a_{\max}(0)/\sqrt{2^m}$ so that $\tau = 4R(0)n_g \Delta t/\delta a_{\max}(0)$ in Eq. (A.1) becomes independent of m. For tumor spheroid growth as well as for blastula formation $R(m)/\delta a_{\max}(m)$ must be independent of m, so we may generally set $a_{\max}(m) = a_{\max}(0)/f(m)$ and $R(m) = R(0)/f(m)$ ($f(m) = \sqrt{2^m}$ for the blastula, and $f(m) = 0.95^{-m/3}$ for the growing tumor spheroid.

The scaled time interval becomes

$$\Delta \hat{t} \equiv \frac{\Delta t}{t} = \frac{\delta a_{\max}(0)}{2R(0)n_g} \tag{A.2}$$

For cells subject to EV interactions the cycle time is $\tau_R \geq \tau$.

In the absence of drift the diffusion constant D can be calculated from

$$\langle (\delta r)^2 \rangle = \int r^2 P(\underline{r}) d^d \underline{r} = 2dD\Delta t \tag{A.3}$$

where d is the dimension and $P(\underline{r})$ the probability to find a step of size $\underline{r}$. The integration is performed over a spherical volume of radius $\xi_{\max}(m)$. Assuming an isotropic distribution $P(\underline{r}) = 1/V$ with $V = \int d^d \underline{r}$, we find $D = \xi_{\max}^2/(8\Delta t)$ in

$d = 2$. Non-dimensionalizing all quantities yields

$$\hat{D}(m) = \frac{\hat{\xi}_{\max}(m)^2}{(8\Delta\hat{t})} \tag{A.4}$$

In $d = 3$ the denominator becomes $15\Delta\hat{t}$. So given D, l and τ, $\hat{D}$ is calculated. The step sizes $\xi_{\max}$ should be chosen sufficiently small in order to insure a linear force-velocity relationship. Then $\Delta\hat{t}$ follows from the last equation and, after insertion into the equation for $\Delta\hat{t} = \ldots$, permits to calculate either n_g, if $\delta a_{\max}(0)$ is chosen, or $\delta a_{\max}(0)$, if n_g is chosen. $\delta a_{\max}(0)$ determines the cycle time distribution of an isolated cell so the possible range for $\delta a_{\max}(0)$ is fixed if the cell cycle distribution is known (which is usually not the case). n_g has to be sufficiently large to insure that a cell performs sufficiently many migration trials to be not kinetically trapped in an energetically unfavorable state. We have chosen the number of rotation trials to be as large as the number of migration trials.

If one would still assume the Stokes-Einstein relation were true then D must scale as the inverse cell size, $\hat{\xi}_{\max}(m)^2 \propto 1/R(m)$ hence $\hat{\xi}_{\max}(m)^2 = \hat{\xi}_{\max}(0)^2 f(m)$. However, this relation is very questionable for cells as least in cases where cells can be assumed to perform an active motion.

APPENDIX B: MATHEMATICAL DISCUSSION OF BUCKLING INSTABILITY

The robustness suggests the instability be generic. An explanation can be given by a continuum model as has been briefly outlined in Ref. 114. Connecting the middle-points of the cells in the configurations found in the simulations for $N \geq 4$ we get a one-dimensional closed curve in two dimensions. As in Goldstein and Langer[143] we may parameterize the closed curve by the position vector $\underline{r}(\alpha, t)$ where $\alpha \in [0, 1)$ is a parameter, t is the time. $\underline{r}(\alpha, t)$ is periodic in α, i.e. $\underline{r}(\alpha = 1, t) = \underline{r}(\alpha = 0, t)$, the same holds for all derivatives, i.e. $\frac{\partial \underline{r}(\alpha,t)}{\partial \alpha}|_{\alpha=0} = \frac{\partial \underline{r}(\alpha,t)}{\partial \alpha}|_{\alpha=1}$. Note that $U = \int_0^1 \sqrt{g}\, d\alpha$ where $g = \frac{\partial \underline{r}(\alpha,t)}{\partial \alpha} \frac{\partial \underline{r}(\alpha,t)}{\partial \alpha}$ is the determinant of the metric tensor.

The mechanisms that contributes to the dynamics are (a) local proliferation of arclength due to cell division, (b) stabilization of stretched structures by a bending energy, (c) constant (at least on the average) perimeter if cell division is switched off. We only consider cell configurations which show sufficiently small deviations from a circle which is surely true at the onset of the instability. For such configurations intersections of the curve with itself cannot occur. Thus we can neglect the excluded volume effect which would have to be represented by a term $\sim \int ds' \int ds(\delta(\underline{r}(s) - \underline{r}(s')))$ with the arclength $ds = \sqrt{g}\, d\alpha$ (e.g. Ref. 144).

According to our assumptions (a)–(c) we make the formal ansatz:

$$\zeta \left. \frac{\partial \underline{r}(\alpha, t)}{\partial t} \right|_{\alpha} = -\frac{1}{\sqrt{g}} \frac{\delta F}{\delta \underline{r}} \tag{B.1}$$

where the pre-factor $\frac{1}{\sqrt{g}}$ ensures reparametization invariance and a damping constant (= inverse of the mobility) has been absorbed into the timescale.

Further

$$F = F_0(\alpha, t) - \int_0^1 \Lambda(\alpha, t)\sqrt{g}d\alpha \tag{B.2}$$

where $\Lambda(\alpha, t)$ is a Lagrangian multiplier field which ensures that the condition for the proliferation of length (cf. condition (a)) which will be specified below, is fulfilled.

$$F_0 = \kappa/2 \int_0^1 [(c(\alpha, t) - c_0)^2]\sqrt{g}d\alpha \tag{B.3}$$

is the bending energy ($c(\alpha, t)$ is the local, c_0 the spontaneous curvature). To get a closed set of equations, we have to fix now a condition for the local metric g:

$$\frac{\partial \sqrt{g}}{\partial t} \equiv f(c). \tag{B.4}$$

(In the following, we use $\partial_t \equiv \frac{\partial}{\partial t}$, $\partial_\alpha \equiv \frac{\partial}{\partial \alpha}$, etc.) After performing the variation in Eq. (B.1), we obtain with Eq. (B.4) a set of two equations of motion:

$$\zeta \partial_t \underline{r} = \left[\frac{\kappa}{2}(c^3 - cc_0^2 + 2\partial_s^2 c) + \Lambda c \right] \underline{n} - \partial_s \Lambda \underline{t} \tag{B.5}$$

and

$$\zeta \frac{\partial \sqrt{g}}{\partial t} = \sqrt{g} \left(\frac{\kappa}{2}[c^4 - c^2 c_0^2 + 2c\partial_s^2 c] + \Lambda c^2 - \partial_s^2 \Lambda \right)$$

$$\equiv f(c) \tag{B.6}$$

with $\underline{n}$ being the local normal and $\underline{t}$ the local tangent to the curve. The normal is directed outward. By the transformation $\lambda \equiv \Lambda - \kappa/2 c_0^2$, one can absorb the spontaneous curvature into the Lagrangian, i.e., in $d = 2$ dimensions, the physics is independent of a global spontaneous curvature (this has also been found for a stability analysis of two-dimensional vesicles by Seifert[145]). To study perturbations of the homogeneous solutions it is convenient to turn to polar coordinates (r, θ), and present r and λ as functions of θ, t, i.e. $r = r(\theta, t)$, $\lambda = \lambda(\theta, t)$ with $\theta \in [0, 2\pi)$. Now $ds = \sqrt{r^2 + (\partial_\theta r)^2}\, d\theta$ and the boundary conditions read $r(\theta = 0, t) = r(\theta = \pi, t)$ and $\partial_\theta r(\theta, t)|_{\theta=0} = \partial_\theta r(\theta, t)|_{\theta=\pi}$. The homogeneous solution is then given by:

$$\zeta \partial_t r = f(c) \tag{B.7}$$

To understand the meaning of $f(c)$, we make the transformation $\tilde{\lambda} \equiv \Lambda - \frac{f(c)}{\sqrt{g}c^2}$, thus Eq. (B.5) becomes

$$\partial_t \underline{r} = \left[\frac{\kappa}{2} \left(c^3 + 2\partial_s^2 c \right) + \tilde{\lambda}c + \frac{f(c)}{\sqrt{g}c} \right] \underline{n} - \partial_s \left(\tilde{\lambda} + \frac{f(c)}{\sqrt{g}c^2} \right) \underline{t}. \qquad \text{(B.8)}$$

The term $\mathcal{G}_n \equiv \frac{f(c)}{\sqrt{g}c}$ describes the growth normal to the line. Here, $\tilde{\lambda}$ insures the conservation of arclength and has been separated from the term that is responsible for the growth. In the regime where $U \propto t^{0.5}$ a cell performs a growth step into the direction of the local normal with a probability proportional to the opening angle β to its neighbors (Fig. 11C). For small angles, β can be shown to correspond to the product of the local curvature with the cell-cell distance in lowest order of a Taylor expansion, i.e., local length proliferation due to cell division corresponds to a negative line tension ($\sim c(\alpha, t)l(\alpha, t)\underline{n}$; note that for non-conserved mass the cell-cell distance, $l(\alpha, t) \approx constant$ and can be absorbed in the growth rate while for total conserved mass $l(\alpha, t) \sim 1/(\sqrt{2})^{m(\alpha,t)}$, where $m(\alpha, t)$ is the generation of the cell at position α. For synchronized cell division $m(t) = \log(N(t))/\log(2)$ thus $l \sim 1/\sqrt{N}$ independent of α.). Comparison with Eq. (B.8) leads to $f(c) = \sigma \sqrt{g}c^2$ where σ is a growth rate. For the homogeneous case, this corresponds to $f(c) = 1/r$ thus $r \sim \sqrt{t}$. This is the result found in the simulations (Fig. 18(B–D)). In the exponential growth regime, the ansatz $f(c) = \sigma_0\sqrt{g}$ yields $r \sim \exp\{\sigma_0 t\}$ i.e., exponential growth as observed in Fig. 18A. A general ansatz may hence be $f(c) = \sigma_k \sqrt{g}c^{2k}$ with ($k = 0, 1, 2, \ldots$). In the following we linearize around the homogeneous state. From Eq. (B.6) it is obvious that the dynamics of Λ is determined by that of r. Now we linearizing around $r = r_0(t)$, $\Lambda = \Lambda_0 = \frac{1}{2}(-\kappa/r_0^2 + \kappa c_0^2) + \sigma$ where r_0 is the solution of $dr_0/dt = \sigma/r_0$ by the ansatz $r(\theta, t) = r_0(t) + \delta r(\theta, t)$ and $\Lambda(\theta, t) = \Lambda_0 + \delta\Lambda(\theta, t)$. With $\delta r(\theta, t) = \xi(t)\exp(im\theta)$ $(m = 0, 1, 2, 3, \ldots.)$, $\delta\Lambda(\theta, t) = \eta(t)\exp(iq\theta)$ $(q = 0, 1, 2, 3, \ldots.)$, and taking into account $q = m \forall m, q$ (because the dynamics of Λ follows that of r) we obtain with $\xi(t) \sim \xi_0 \exp(w(q)t)$ the dispersion relation

$$w(q) = -\frac{\kappa q^6 - q^4(\sigma r_0^2 + 2\kappa) + \kappa q^2 + \sigma r_0^2}{(1 + q^2)r_0^4} = -\frac{\kappa q^2(q^2 - 1)^2 - \sigma r_0^2(q^4 - 1)}{(1 + q^2)r_0^4} \qquad \text{(B.9)}$$

The mode $q = 0$ has the equation $w(0) = -\sigma/r_0^2$ which means, that every homogeneous perturbation would be damped out compared to the unperturbed homogeneous perturbation (the $q = 0$-mode doesn't measure changes with respect to a stationary but to a homogeneous solution which grows itself, so the difference decreases with time after a perturbation. The direction of movement does even not change if $w(0)$ would be positive). $w(q = 1) = 0$: Up to linear order, the $q = 1$-mode describes a translation of the circle which is marginally stable.[145] Note that for the general growth function $f(c) = \sigma_k\sqrt{g}c^{2k}$

$(k = 0, 1, 2, \ldots), (q^4 - 1) \rightarrow (q^2 - 1)(q^2 - 1 + 2k)$ in the numerator of the 2nd. term on the rhs. of Eq. (B.9). For $q^2 \gg \max(1, 2k - 1)$, $\omega(q) \approx -Aq^4 + Bq^2$ with $A = \kappa/(r_0^4 \zeta)$, $B = \sigma_k/r_0^{2k}$ (for $q \gg 1$) one obtains a dispersion relation as for particular cases of dendrite growth.[146] If no growth occurs ($\sigma_k = 0$) the circle is the only stable solution. Otherwise, $\omega(q = 0) = \sigma_0 > 0$ for exponential growth, so homogeneous deviations grow. For the power-law growth regime $U \propto t^{0.5}$, $\omega(0) = -\sigma_1/r_0^2$, so homogeneous perturbations are damped out. $\omega(q = 1) = 0$, a translation of the circle is marginally stable[145] (compare above). ω has a second zero at $q_c^2 = X$ for $\kappa = 0$ and $q_c^2 = [1 + X + \{(1 - X)^2 + 8Xk\}^{0.5}]/2$ for $k > 0$, with $X \equiv B/A = \zeta \sigma_k r_0^{4-2k}/\kappa$. For $1 < q < q_c$, $\omega(q) > 0$. For $q \rightarrow \infty$, $\omega(q) < 0$, i.e., short wavelength perturbations are damped out. The fastest growing mode is $q_m^2 \approx X/2$ (if $q_m \gg 1$). q_c and q_m grow with increasing X. The buckling insta- bility occurs at domain sizes $\propto q_c^{-1}$ that decrease with increasing growth strength and decreasing bending rigidity, in agreement with the tendencies found in the computer simulations.

In the computer simulations we observed in the power-law growth regime that the buckling occurs at domain sizes that increase with τ and κ and decrease with ϵ. This can be qualitatively understood as follows: The larger κ is, the better is the bending energy able to damp out small deviations of the cell configuration from a perfect circle. A large cycle time has the same effect: the cell configuration has more time to relax into the minimum energy configuration. A large ϵ has the opposite effect. The nearest-neighbor energy is minimized if cells avoid configu- rations where the distance between nearest neighbors falls below the equilibrium value, e.g. by increasing small deviations perpendicular to the circular configura- tion. These are disfavored by the bending energy which decreases as $1/r$. Hence the larger ϵ is the earlier the bending energy becomes unable to balance the energy increase of nearest-neighbor energy. It is possible to analytically calculate the point at which the buckling instability occurs within the power-law growth regime based on a Langevin equation for each cell and the assumption that buckling occurs if the bending force becomes of the same order as the de-stabilizing forces due to cell growth and division.

ACKNOWLEDGMENT

REFERENCES

1. S. Huang and D. Ingber, The structural and mechanical complexity of cell-growth control. *Nature Cell Biol.* **1**:E131 (1999).
2. I. Salazar-Ciudad, J. Jernvall, and S. A. Newman, Mechanisms of pattern formation in development and evolution. *Development* **130**:2027 (2003).
3. D. J. Tschumperlin, EGFR autocrine signaling in a compliant interstitial space: Mechanotransduction from the outside in. *Cell Cycle* **3**:996 (2004).
4. A. Neagu, K. Jakab, R. Jamison, and G. Forgacs, Role of physical mechanisms in biological self-organization. *Phys. Rev. Lett.* **95**:178104 (2005).
5. G. Forgacs and S. Newmann, *Biological Physics of the Developing Embryo* (Cambridge University Press, Cambridge, 2005).
6. G. Helmlinger, P. Netti, H. Lichtenfeld, R. Melder, and R. Jain, Solid stress inhibits the growth of multicellular tumor spheroids. *Nature Biotechnol.* **15**:778 (1997).
7. C. Nelson, R. Jean, J. Tan, W. Liu, N. Sniadecki, A. Spector, and C. Chen, Mechanical control of tissue growth: Function follows form. *Proc. Natl. Acad. Sci. (USA)*, **102**:(2005).
8. D. Ingber, Mechanical control of tissue morphogenesis during embryological development. *Int. J. Dev. Biol.* **50**:255 (2006).
9. D. Ingber, Mechanical control of tissue growth: Function follows form. *Proc. Natl. Acad. Sci. (USA)* **102**:11571 (2005).
10. L. D. Horb and J. M. Slack, Role of cell division in branching morphogenesis and differentiation of the embryonic pancreas. *Int. J. Dev. Biol.* **44**:791 (2000).
11. B. Shraiman, Mechanical feedback as a possible regulator of tissue growth. *Proc. Natl. Acad Sci. (USA)* **102**:3318 (2005).
12. H. Lodish, A. Berk, P. Matsudaria, C. Kaiser, M. Krieger, M. Scott, S. Zipursky, and J. Darnell, *Molecular Cell Biology* (Freeman, New York, 2004).
13. H. Byrne, J. King, D. McElwain, and L. Preziosi, A two-phase model of solid tumor growth, *Appl. Math. Lett.*, pp. 1–15 (2001).
14. C. Chen, H. Byrne and J. King, The influence of growth-induced stress from the surrounding medium on the development of multicell spheroids, *J. Math. Biol.* **43**:191 (2001).
15. U. Schwarz, N. Balaban, D. Riveline, A. Bershadsky, B. Geiger, and S. Safran, Calculation of forces at focal adhesions from elastic substrate data: The effect of localized force and the need for regularization, *Biophys. J.* **83**:1380 (2002).
16. H. Byrne and L. Prezziosi, Modelling solid tumour growth using the theory of mixtures, *Math. Med. Biol.* **20**:341 (2003).
17. I. Bischofs and U. Schwarz, Effect of poisson ratio on cellular structure formation. *Phys. Rev. Lett.* **95**:068102 (2005).
18. I. Schiffer, S. Gebhard, C. Heimerdinger, A. Heling, J. Hast, U. Wollscheid, B. Seliger, B. Tanner, S. Gilbert, T. Beckers, S. Baasner, W. Brenner, C. Spangenberg, D. Prawitt, T. Trost, W. Schreiber, B. Zabel, M. Thelen, H. Lehr, F. Oesch, and J. Hengstler, Switching off her-2/ neu in a tetracycline-controlled mouse tumor model leads to apoptosis and tumorsize-dependent remission. *Cancer Res.* **63**:7221 (2003).
19. M. Alison and C. Sarraf, *Understanding Cancer* (Cambridge University Press, Cambridge, 1998).
20. B. Sayan, G. Ince, A. Sayan, and M. Ozturk, Napo as a novel apoptosis marker. *J. Cell Biol.* **155**:719 (2001).
21. J. Mombach and J. Glazier, Single cell motion in aggregates of embryonic cells. *Phys. Rev. Lett.* **76**:3032 (1996).
22. J. Guck, R. Ananthakrishnan, H. Mahmood, T. Moon, C. Cunningham and J. Käs, The optical stretcher: A novel laser tool to micromanipulate cells. *Biophys. J.* **81**:767 (2001).

23. J. Alcaraz, L. Buscemi, M. Grabulosa, X. Trepat, B. Fabry, R. Farre, and D. Navajas, Microrheology of human lung epithelial cells measured by atomic force microscopy. *Biophys. J.* **84**:2071 (2003).

24. C. Laforsch, W. Ngwa, W. Grill, and R. Tollrian, An acoustic microscopy technique reveals hidden morphological defenses in daphnia. *Proc. Natl. Acad. Sci. (USA)* **101**:15911 (2005).

25. S. Chesla, P. Selvaraj and C. Zhu, Measuring two-dimensional receptor-ligand binding kinetics by micropipette. *Biophys. J.* **75**:1553 (1998).

26. X. Zhang, A. Chen, D. Leon, H. Li. E. Noiri, V. Moy, and M. Goligorsky, Atomic force microscopy measurement of leukocyte-endothelial interaction. *Am. J. Physiol. Heart Circ. Physiol.* **286**:H359 (2004).

27. J. Galle, G. Aust, G. Schaller, T. Beyer, and D. Drasdo, Single-cell based mathematical models to the spatio-temporal pattern formation in multi-cellular systems, Cytometry A, in press (2006).

28. U. Braumann, J. Kuska, J. Einenkel, L. Horn, M. Loeffler, and M. Hoeckel, Three-dimensional reconstruction and quantification of cervical carcinoma invasion fronts from histological serial sections. *IEEE Trans. Med. Imaging* **24**:1286 (2005).

29. D. Helbing, Traffic and related self-driven many particle systems. *Rev. Mod. Phys.* **73**:1067 (2001).

30. D. Drasdo, R. Kree and J. McCaskill, Monte-carlo approach to tissue-cell populations. *Phys. Rev. E* **52**:6635 (1995).

31. J. Moreira and A. Deutsch, Cellular automata models of tumour development—a critical review. *Adv. Complex Syst.* **5**: 247 (2002).

32. M. S. Alber, M. A. Kiskowski, J. A. Glazier, and Y. Jiang, On cellular automaton approaches to modeling biological cells. In *Mathematical Systems Theory in Biology, Communication, and Finance*, J. Rosenthal and D. S. Gilliam (eds.) (IMA 142, Springer-Verlag, New York, 2002), pp. 1–40.

33. D. Drasdo, On selected individual-based approaches to the dynamics of multicellular systems. In *Multiscale modeling*, J. L. W. Alt and M. Griebel (eds.) (Birkhäuser, 2003).

34. T. Cickovski, C. Huang, R. Chaturvedi, T. Glimm, H. Hentschel, M. Alber, J. A. Glazier, S. A. Newman, and J. A. Izaguirre, A framework for three-dimensional simulation of morphogenesis. *IEEE/ACM Trans. Comput. Biol. Bioinformatics* **2**:273 (2005).

35. R. Merks and J. Glazier, A cell-centered approach to developmental biology. *Physica A* **352**:113 (2005).

36. A. Bru, J. Pastor, I. Fernaud, I. Bru, S. Melle, and C. Berenguer, Super-rough dynamics of tumor growth. *Phys. Rev. Lett.* **81**:4008 (1998).

37. D. Balkovetz, Evidence that hepatocyte growth factor abbrogates contact inhibition of mitosis in madin-darby canine kidney cell monolayers. *Life Sci.* **64**:1393 (1999).

38. L. Kunz-Schughart, Multicellular tumor spheroids: Intermediates between monolayer culture and in-vivo tumor. *Cell Biol. Int.* **23**:157 (1999).

39. M. Locke, M. Heywood, S. Fawell, and I. Mackenzie, Retention of intrinsic stem cell hierarchies in carcinoma-derived cell lines. *Cancer Res.* **65**:8944 (2005).

40. W. Mueller-Klieser, A review on cellular aggregates in cancer research. *Cancer Res. Clin. Oncol.* **113**:101 (1987).

41. R. Sutherland, Cell and environment interactions in tumor microregions: The multicell spheroid model. *Science* **240**:177 (1988).

42. M. Santini and G. Rainaldi, Three-dimensional spheroid model in tumor biology. *Pathobiology* **67**:148 (1999).

43. S. Gilbert, *Develoment* (Sinauer Associates Inc., New York, 1997).

44. L. Wolpert, *Principles of Development* (Oxford Univ. Press, Oxford, 1998).

45. C. Booth and C. Potten, Gut instincts, thoughts on intestinal epithelial stem cells. *Clin. Invest.* **105**:1493 (2000).

46. C. Potten and M. Loeffier, Stem cells: Attributes, cycles, spirals, pitfalls and uncertainties. Lessons for and from the crypt. *Development* **110**:1001 (1990).
47. D. Drasdo and M. Löffler, Individual-based models on growth and folding in one-layered tissues: Intestinal crypts and blastulation. *Nonl. Anal.* **47**:245 (2001).
48. C. Farrell, K. Rex, S. Kaufman, C. Dipalma, J. Chen, S. Scully and D. Layey, Effects of keratinocyte growth factor in the squamous epithelium of the upper aero-digestive tract of normal and irradiated mice. *Int. J. Radiat. Biol.* **75**:609 (1999).
49. C. Klein, T. Blankenstein, O. Schmidt-Kittler, M. Petronio, B. Polzer, N. Stoecklein, and G. Riethmuller, Genetic heterogeneity of single disseminated tumour cells in minimal residual cancer. *Lancet* **360**:683 (2002).
50. H. Eagle, Nutrienton needs of mammalian cells in tissue culture. *Science* **122**:43 (1955).
51. R. Ham, Clonal growth of mammalian cells in a chemically defined, synthetic medium. *Proc. Natl. Acad. Sci.* **53**:288 (1965).
52. I. Hayashi and G. Sato, Replacement of serum by hormones permits growth of cells in defined medium. *Nature* **239**:132 (1976).
53. G. Sato, A. Pardee and D. Sirbasku, *Growth of Cells in Hormonally Defined Media* (Cold Spring Harbour Laboratory, 1982).
54. K. Burrige, Substrate adhesions in normal and transformed fibroblasts: Organization and regulation of cytoskeletal, membrane and extracellular matrix components at focal contacts. *Cancer Review* **4**:18 (1986).
55. A. Bru, S. Albertos, J. Subiza, J. Garcia-Arsenio, and I. Bru, The universal dynamics of tumor growth. *Biophys. J.* **85**: 2948 (2003).
56. L. Davidson, M. Koehl, R. Keller, and G. Oster, How do sea urchins invaginate? using biomechanics to distinguish between mechanisms of primary invagination. *Development* **121**:2005 (1995).
57. M. Lekka, P. Laidler, D. Gil, J. Lekki, Z. Stachura, and A. Z. Hrynkiewicz, Elasticity of normal and cancerous human bladder cells studied by scanning force microscopy. *European Biophys. J.* **28**:312 (1999).
58. J. Piper, R. Swerlick and C. Zhu, Determining force dependence of two-dimensional receptorligand binding affinity by centrifugation. *Biophys. J.* **74**:492 (1998).
59. D. Beysens, G. Forgacs, and J. Glazier, Cell sorting is analogous to phase ordering in fluids. *Proc. Natl. Acad. Sci. USA* **97**:9467 (2000).
60. M. Schienbein, K. Franke, and H. Gruler, Random walk and directed movement: Comparison between inert particles and self-organized molecular machines. *Phys. Rev. E* **49**:5462 (1994).
61. R. A. Gatenby and P. K. Maini, Mathematical oncology: Cancer summed up. *Nature* **421**:321 (2003).
62. J. Fidorra, T. Mielke, J. Booz, and L. Feinendegen, Cellular and nuclear volume of human cells during cell cycle. *Radiat. Environ. Biophys.* **19**:205 (1981).
63. D. Landau, *Theory of elasticity* (Pergamon, 1975).
64. R. Carpick, D. F. Ogletree, and M. Salmeron, A gerneral equation for fitting contact area and friction vs. load measurements. *J. Colloid Interface Sci.* **211**:395 (1999).
65. Y.-S. C. *et al.*:Johnson-kendall-roberts theory applied to living cells. *Phys. Rev. Lett.* **280**:312 (1999).
66. D. Drasdo and S. Hoehme, A single-cell based model to tumor growth in-vitro: Monolayers and spheroids. *Phys. Biol.* **2**:133 (2005).
67. N. Metropolis, A. Rosenbluth, M. Rosenbluth, A. Teller, and E. Teller, Equation of state calculations by fast computing machines. *J. Chem. Phys.* **21**:1087 (1953).
68. D. Drasdo and G. Forgacs, Modelling the interplay of generic and genetic mechanisms in cleavage, blastulation and gastrulation. *Dev. Dyn.* **219**:182 (2000).

69. D. Drasdo and S. Höhme, Individual-based approaches to birth and death in avascular tumors. *Math. and Comp. Modelling* **37**:1163 (2003).

70. M. Allen and D. Tildersley, *Computer Simulation of Liquids* (Oxford Science Publ., Oxford, 1987).

71. D. Landau and K. Binder, *A Guide to Monte Carlo Simulations in Statistical Physics* (Cambridge University Press, 2000).

72. M. Eden, A two-dimensional growth process. In *Proceedings of the 4th. Berkeley Symposium on Mathematics and Probability*, vol. IV, J. Neyman (ed.) (University of California Press, 1961), pp. 223–239.

73. R. Weinberg, *The biology of cancer* (Garland Science, New York and Oxford, 2007).

74. J. Xin, Front propagation in heterogeneous media. *SIAM Rev.* **42**:161 (2000).

75. K. Swanson, E. Alvord, and J. Murray, quantitativ model for differential motility of gliomas in gey and white matter. *Cell Prolif.* **33**:317 (2000).

76. B. Alberts, A. Johnson, J. Lewis, M. Raff, K. Roberts, and P. Walter, *The cell* (Garland Science Publ., New York, 2002).

77. J. Galle, M. Loeffler, and D. Drasdo, Modelling the effect of deregulated proliferation and apoptosis on the growth dynamics of epithelial cell populations in-vitro. *Biophys. J.* **88**: 62 (2005).

78. G. Schaller and M. Meyer-Hermann, Multicellular tumor spheroid in an off-lattice voronoi-delaunay cell model. *Phys. Rev. E.* **71**:051910 (2005).

79. J. Piper, R. Swerlick, and C. Zhu, Determining force dependence of two-dimensional receptorligand binding affinity by centrifugation. *Biophys. J.* **74**:492 (1998).

80. J. Dhont, *An introduction to dynamics of colloids* (Elsevier, Amsterdam, 1996).

81. L. Li, J. Backer, A. Wong, E. Schwanke, B. Stewart, and M. Pasdar, Bcl-2 expression decreases cadherin-mediated cell-cell adhesion. *J. Cell Sci.* **116**:3687 (2003).

82. M. Warchol, Cell density and n-cadherin interaction regulates cell proliferation in the sensory epithelia of the inner ear. *J. Neurosci.* **22**:2607 (2002).

83. P. Klekotka, S. Santoro, A. Ho, S. Dowdy, and M. Zutter, Mammary epithelial cell-cycle progression via the $\alpha 2\beta 1$-integrin. *Am. J. Path.* **159**:983 (2001).

84. L. Junqueira and J. Carneiro, *Basic histology* (McGraw Hill, 2005).

85. D. Stupack and D. Cheresh, Get a ligand, get a life: Integrins, signaling and cell survival. *J. Cell Sci.* **115**:3729 (2002).

86. K. Orford. C. Orford, and S. W. Byers, Exogenous expression of β-catenin regulates contact inhibition, anchorage-independent growth, anoikis and radiation-induced cell cycle arrest. *J. Cell Biol.* **146**:855 (1999).

87. Z. Yan, M. Chen, M. Perucho, and E. Friedman, Oncogenic ki-ras but not oncogenic ha-ras blocks integrin? 1-chain maturation in colon epithelial cells. *J. Biol. Chem.* **272**:2607 (1997).

88. P. Lu, Q. Lu, A. Rughetti, and J. Taylor-Papadimitriou, bcl-2 overexpression inhibits cell death and promotes the morphogenesis, but not tumorigenesis of human mammary epithelial cells. *J. Cell Biol.* **129**:1363 (1995).

89. R. Bates, N. Edwards, and J. Yates, Spheroids and cell survival. *Crit. Rev. Oncol./Hematol.* **36**:61 (2000).

90. M. Santini, G. Rainaldi, and P. Indovina, Apoptosis, cell adhesion and the extracellular matrix in the three-dimensional growth of multicellular tumor spheroids. *Crit. Rev. Oncology/Hematology* **36**:75 (2000).

91. C. Chen, M. Mrksich, S. Huang, G. Whitesides, and D. Ingber, Geometric control of cell life and death. *Science* **276**: 1425 (1997).

92. N. Gloushankova, N. Alieva, M. Krendel, E. Bonder, H. Feder, J. Vasiliev, and I. Gelfand, Cell-cell contact changes the dynamics of lamellar activity in nontransformed epitheliocytes but not in their ras-transformed descendants. *Proc. Natl. Acad. Sci. USA* **94**:879 (1997).

93. A. Barabasi and H. Stanley, *Fractal concepts in surface growth* (Cambridge University Press, Cambridge, 1995).
94. E. Moro, Internal fluctuations effects on fisher waves. *Phys. Rev. Lett.* **87**:238303 (2001).
95. T. Halpin-Healy and Y. Zhang, Kinetic roughening phenomena, stochastic growth, directed polymers and all that. *Phys. Rep.* **254**:215 (1995).
96. M. Block, E. Schoell, and D. Drasdo, Classifying the expansion kinetics and critical surface dynamics of growing cell populations, *Cond. mat. physics*/0610146 (2006).
97. D. Drasdo, Coarse graining in simulated cell populations. *Adv. Complex Syst.* **8**:319 (2005).
98. J. Ramasco, J. Lopez, and M. Rodriguez, Generic dynamic scaling in kinetic roughening. *Phys. Rev. Lett.* **84**:2199 (2000).
99. F. Family and T. Vicsek, Scaling of the active zone in the eden process on percolation networks and the ballistic deposition model. *J. Phys. A: Math. Gen.* **18**:L75 (1985).
100. J. Buceta and J. Galeano, Comments on the article—the universal dynamics of tumor growth. *Biophys. J.* **88**:3734 (2005).
101. A. Wong and B. Gumbiner, Adhesion-independent mechanism for suppression of tumor cell invasion by e-cadherin. *J. Cell Biol.* **161**:1191 (2003).
102. P. Friedl, Prespecification and plasticity: Shifting mechanisms of cell migration. *Curr. Opin. Cell. Biol.* **16**:14 (2004).
103. J. Freyer and R. Sutherland, A reduction in the in situ rates of oxygen and glucose consumption of cells in emt6/ro spheroids during growthregulation of growth. *J. Cell. Physiol.* **124**:516 (1985).
104. J. Freyer and R. Sutherland, Regulation of growth saturation and development of necrosis in emt6/ro multicellular spheroids by the glucose and oxygene supply. *Cancer Res.* **46**:3504 (1986).
105. J. Casciari, S. Sotirchos, and R. Sutherland, Glucose diffusivity in multicellular tumor spheroids. *Cancer Res.* **48**:3905 (1988).
106. J. Casciari, S. Sotirchos, and R. Sutherland, Variations in tumor cell growth rates and metabolism with oxygen concentration, glucose concentration and extracellular ph. *J. Cell. Physiol.* **151**:386 (1992).
107. Y. Jiang, J. Pjesivac-Grbovic, C. Cantrell, and J. Freyer, A multiscale model for avascular tumor growth. *Biophys. J.* **89**:3884 (2005).
108. E. Stott, N. Britton, J. Glazier, and M. Zajac, Stochastic simulation of benign avascular tumor growth using the potts model. *Math. Comput. Modelling* **30**:183 (1999).
109. S. Dormann and A. Deutsch, Modeling of self-organized avascular tumor growth with a hybrid cellular automaton. *Silico Biol.* **2**:0035 (2002).
110. J. Folkman and M. Hochberg, Self-regulation of growth in three dimensions. *J. Exp. Med.* **138**:745 (1973).
111. J. Glazier and F. Graner, Simulation of the differential adhesion driven rearrangement of biological cells. *Phys. Rev. E* **47**:2128 (1993).
112. T. Newman, Modeling multi-cellular systems using sub-cellular elements. *Math. Biosciences Eng.* **2**:613 (2005).
113. N. Wright and M. Alison, *The Biology of Epithelial Cell Population* (Clarendon Press, Oxford, 1984).
114. D. Drasdo, Buckling instabilities in one-layered growing tissues. *Phys. Rev. Lett.* **84**:4244 (2000).
115. S. Hörstadius, The mechanics of sea urchin development, studied by operative methods. *Biol. Rev.* **14**:132 (1939).
116. K. Dan, Cytoembryology of echinoderms and amphibia. *Int. Rev. Cytol* **9**:321 (1960).
117. L. Wolpert and E. Mercer, An electron microscope study of the development of the blastula of the sea urchin embryo and its radial polarity. *Exp. Cell Res.* **30**:280 (1963).
118. M. Leptin and B. Grunewald, Cell shape changes during gastrulation in drosophila. *Development* **110**:73 (1990).

119. J. Gere and S. Timoshenko, *Mechanics of Materials*, 4th edn. (PWS-Publishing Co., Boston, 1997).
120. J. Dallon and H. Othmer, How cellular movement determines the collective force generated by the dictyostelium discoideum slug. *J. theor. Biol.* **231**:203 (2004).
121. E. Palsson and H. Othmer, A model for individual and collective cell movement in dictyostelium discoideum. *Proc. Natl. Acad. Sci. USA* **12**:10448 (2000).
122. Z. Kam, J. Minden, D. Agard, J. Sedat, and M. Leptin, Drosophila gastrulation: Analysis of cell shape changes in living embryos by three-dimensional fluorescence mircroscopy. *Development* **112**:365 (1991).
123. A. Cairnie and B. Millen, Fission of crypts in the small intestine of the irradiated mouse. *Cell Tissue Kinet.* **8**:89 (1975).
124. K. Araki, T. Ogata, M. Kobayashi, and R. Yatani, A morphological study on the histogenesis of human colorectal hyperplastic crypts. *Gastroenterology* **109**:1468 (1995)
125. A. Bru, S. Albertos, J. L. Garcia-Asenjo, and I. Bru, Pinning of tumoral growth by enhancement of the immune response. *Phys. Rev. Lett.* **92**:238101 (2004).
126. Y. Boucher, L. Baxter, and R. Jain, Interstitial pressure gradients in tissue-isolated and subcutaneous tumors: Implications for therapy. *Cancer Res.* **50**:4478 (1990).
127. Y. Boucher, J. Salehi, B. Witwer, and R. Jain, Interstitial fluid pressure in intracranial tumors in patients and in rodents. *Br. J. Cancer* **75**:829 (1997).
128. E. Filipski, F. Delaunay, V. King, B. C. MW Wu, A. Grechez-Cassiau, C. Guettier, M. Hastings, and F. Levi, Effects of chronic jet lag on tumor progression in mice. *Cancer Res.* **64**:7879 (2004).
129. A. Goriely and M. B. Amar, Differential growth and instability in elastic shells. *Phys. Rev. Lett.* **94**:198103 (2005).
130. J. Dunphy, *Wound healing* (MedCom-Press, New York, 1978).
131. P. Hogeweg, Evolving mechanisms of morphogenesis: On the interplay between differential adhesion and cell differentiation. *J. Theor. Biol.* **203**:317 (2000).
132. D. Drasdo and M. Kruspe, Emergence of cell migration and aggregation strategies in a simulated evolutionary process. *Adv. Complex Syst.* **8** (2005).
133. T. Alarcon. H. Byrne, and P. Maini, A mathematical model of the effects of hypoxia on the cell-cycle of normal and cancer cells. *J. Theor. Biol.* **229**:395 (2004).
134. K. Frame and W. Hu, A model for density-dependent growth of anchorage-dependent mammalian cells. *Biotechnol. Bioengineering* **32**:1062 (1988).
135. K. Hawboldt, N. Kalogerakis, and L. Behie, A cellular automaton model for micro-carrier cultures. *Biotechnol. Bioengineering* **43**:90 (1993).
136. L. Arakelyan, Y. Merbl, and Z. Agur, Vessel maturation effects on tumour growth: Validation of a computer model in implanted human ovarian carcinoma spheroids. *Eur. J. Cancer* **41**:159 (2005).
137. C. Basdevant, J. Clairambault, and F. Levi, Optimisation of time-scheduled regimen for anti-cancer drug infusion. *Math. Modelling Numerical Anal.* **39**:1069 (2005).
138. B. Ribba, K. Marron, Z. Agur, T. A. T, and P. Maini, A mathematical model of doxorubicin treatment efficacy for non-hodgkin's lymphoma: Investigation of the current protocol through theoretical modelling results. *Bull. Math. Biol.* **67**:79 (2005).
139. B. Ribba, T. Colin, and S. Schnell, A multiscale mathematical model of cancer and its use in analyzing irradiation therapies. *Theor. Biol. Med. Model* **3**:7 (2006).
140. N. Grabe and K. Neuber, A multicellular systems biology model predicts epidermal morphology, kinetics and ca$^+$-flow. *Bioinformatics* **21**:3541 (2005).
141. S. Hoehme, J. Hengstler, M. Brulport, M. Schaefer, A. Bauer, R. Gebhardt, and D. Drasdo, Mathematical modelling of liver regeneration after intoxification with CCl$_4$, Chemico-Biological Interactions, accepted for publication (2007).
142. G. Michalopoulos and M. DeFrances, Liver regeneration. *Science* **276**:60 (1997).

143. R. Goldstein and S. Langer, Nonlinear dynamics of stiff polymers. *Phys. Rev. Lett.* **75**:1094 (1995).
144. M. Doi and S. F. Edwards, *The theory of polymer dynamics* (Oxford University Press, 1986).
145. U. Seifert, Adhesion of vesicles in two dimensions. *Phys. Rev. A* **43**:6803 (1991).
146. D. Kessler, J. Koplik, and H. Levine, Pattern selection in fingered growth, phenomena. *Adv. Phys.* **37**:255 (1988).